

Evaluation of scale-aware subgrid mesoscale eddy models in a global eddy-rich model



Brodie Pearson^{a,1,*}, Baylor Fox-Kemper^a, Scott Bachman^b, Frank Bryan^c

^a Department of Earth, Environmental and Planetary Science, Brown University, Providence, USA

^b Department of Applied Mathematics and Theoretical Physics, University of Cambridge, UK

^c NCAR, Boulder, USA

ARTICLE INFO

Article history:

Received 30 November 2016

Revised 31 March 2017

Accepted 17 May 2017

Available online 18 May 2017

Keywords:

Mesoscale eddies
Large eddy simulation
Global climate models
Subgrid models

ABSTRACT

Two parameterizations for horizontal mixing of momentum and tracers by subgrid mesoscale eddies are implemented in a high-resolution global ocean model. These parameterizations follow on the techniques of large eddy simulation (LES). The theory underlying one parameterization (2D Leith due to Leith, 1996) is that of enstrophy cascades in two-dimensional turbulence, while the other (QG Leith) is designed for potential enstrophy cascades in quasi-geostrophic turbulence. Simulations using each of these parameterizations are compared with a control simulation using standard biharmonic horizontal mixing.

Simulations using the 2D Leith and QG Leith parameterizations are more realistic than those using biharmonic mixing. In particular, the 2D Leith and QG Leith simulations have more energy in resolved mesoscale eddies, have a spectral slope more consistent with turbulence theory (an inertial enstrophy or potential enstrophy cascade), have bottom drag and vertical viscosity as the primary sinks of energy instead of lateral friction, and have isoneutral parameterized mesoscale tracer transport. The parameterization choice also affects mass transports, but the impact varies regionally in magnitude and sign.

© 2017 Elsevier Ltd. All rights reserved.

1. Introduction

Mesoscale eddies are a ubiquitous component of the dynamical ocean system. These eddies mix momentum and tracers along isopycnal surfaces², contain a substantial fraction of the ocean's kinetic energy, and can act as a source or sink of energy for fronts and the mean flow. Standard resolution ocean models, such as those used in recent IPCC reports (horizontal resolution $\Delta_h \geq 1^\circ$), cannot resolve mesoscale eddies, but the next generation of ocean models ($\Delta_h \ll 1^\circ$) can resolve the largest mesoscale eddies across much of the global ocean. The former, 'coarse resolution', models must parameterize the effects of all mesoscale eddies, while the latter, 'eddy-resolving', models need only parameterize the effects of unresolved eddies and smaller phenomena, such as boundary layer turbulence (Large et al., 1994), breaking internal waves

(MacKinnon et al., 2013) and submesoscale eddies (Fox-Kemper et al., 2011).

Increasing horizontal resolution to resolve mesoscale eddies has led to increased realism in ocean models (Smith et al., 2000; Roberts et al., 2004; Maltred and McClean, 2005; Hallberg and Gnanadesikan, 2006; Kirtman et al., 2012; Graham, 2014; Jansen et al., 2015b), and shows potential for improving the coupling of the ocean to other components of the Earth system (Hallberg and Gnanadesikan, 2006; Frenger et al., 2013; Bryan et al., 2014). The positive effects of resolving mesoscale eddies emphasize the importance of simulating these eddies with high fidelity, and part of this challenge is to accurately parameterize the effects of unresolved mesoscale eddies.

The strength of horizontal mixing by unresolved mesoscale eddies is typically parameterized through an eddy viscosity (ν) and diffusivity (κ , perhaps paired with related advective transport), which represent eddy stresses and tracer fluxes, respectively. There are two primary factors motivating the choice of ν and κ , and the form of the mixing parameterization. First, the parameterization should represent the primary physical effects of unresolved mesoscale eddies. Second, the mixing must be strong enough to maintain numerical stability by damping extreme events (Griffies and Hallberg, 2000; Lucas et al., 2013), but not so strong as to

* Corresponding author.

E-mail addresses: brodie_pearson@brown.edu, brodiecraigpearson@gmail.com
(B. Pearson).

¹ Present Address: Department of Earth, Environmental and Planetary Science, Brown University, Providence, RI 02906, USA.

² More precise statements of energy constraints can be found elsewhere (McDougall, 1987; Young, 2010; Nylander, 2011), here we use along-isopycnal as a shorthand for a more complete description.

over-damp the resolved flow (Delworth et al., 2012; Hallberg, 2013; Jansen and Held, 2014). Many parameterizations assume that mixing occurs across gradients and acts through a Laplacian operator in a manner analogous to molecular (Fickian) diffusion; e.g. $\nabla_h \cdot (\nu \nabla_h \phi)$, where ϕ is the diffused property and the subscript h denotes horizontal derivatives. There are also parameterizations based on higher-order derivatives such as biharmonic operators ($\nu \nabla_h^4 u$; Semtner and Mintz, 1977), which aim to damp the flow at smaller scales than Laplacian operators. Finally, some mixing schemes pay particular attention to reducing mixing across isopycnals (Redi, 1982; Gent and McWilliams, 1990), but these schemes are rarely used in eddy-resolving models (Roberts and Marshall, 1998). In both eddy-resolving and coarse resolution models, the ocean structure is affected by the choice of both ν (Griffies et al., 2000; Smith and McWilliams, 2003; Bryan et al., 2007; Jochum et al., 2008; Ilicak et al., 2012; Arbic et al., 2013) and κ (Maes et al., 1997; Gent et al., 2001; Pezzi and Richards, 2003; Kuhlbrodt et al., 2012).

Significant spatial variations in the strength of mixing and transport by mesoscale eddies have been seen in observations (Eden, 2007; Chelton et al., 2011; Abernathey and Marshall, 2013; Klocker and Abernathey, 2014) and in eddy-resolving models (Visbeck et al., 1997; Abernathey et al., 2010; Fox-Kemper et al., 2013; Bachman et al., 2015). For example, intense eddy mixing occurs in the Southern Ocean and in Western Boundary Currents (WBCs; Abernathey and Marshall, 2013). These variations in κ occur in both the horizontal and the vertical (Ferreira et al., 2005), and cover more than an order of magnitude (Zhurbas and Oh, 2003; Cole et al., 2015). Including a spatially varying κ in coarse resolution models can significantly improve the resolved flow (Danabasoglu and Marshall, 2007; Eden et al., 2009; Berloff, 2015), and spatially-varying viscosity in simple models may improve their dynamical realism (Fox-Kemper and Pedlosky, 2004; Fox-Kemper, 2004). Pezzi and Richards (2003) show that spatially varying ν and κ are required for their ocean model to be comparable to observations.

In coarse resolution models, viscosity acts horizontally but the mixing of tracers is often oriented along isopycnals using the Gent-McWilliams and Redi parameterizations (Redi, 1982; Gent and McWilliams, 1990). The combined “GM-Redi” parameterization advects and diffuses tracers along isopycnals (Fox-Kemper et al., 2013). The along-isopycnal diffusive component of the parameterization does not affect the density field, but the advective component can re-arrange fluid parcels of different densities and in doing so it converts available potential energy to kinetic energy (Gent et al., 1995; Griffies, 1998). Parameterizing along-isopycnal diffusion of tracers conserves water mass properties and has led to significant improvements in ocean models relative to assuming horizontal diffusion (Veronis, 1975; Danabasoglu and McWilliams, 1995; Lengaigne et al., 2003). Orienting eddy momentum fluxes along isopycnals is not required for dynamics in the quasi-geostrophic regime, as the vertical velocities vanish to leading order and so the covariance corrections are negligible.

The present generation of eddy-resolving models for the global ocean typically have horizontal resolution of $O(1/10^\circ)$ which means that the largest mesoscale eddies (~ 30 km and larger) are resolved almost everywhere (Hallberg, 2013), but the smallest mesoscale eddies are typically less than 10 km and the effects of these unresolved eddies should be parameterized. In eddy-resolving models the values of ν and κ are often chosen for numerical stability and used with a horizontal biharmonic operator rather than the GM-Redi scheme (Maltrud et al., 2010; McClean et al., 2011; Delworth et al., 2012; Bryan et al., 2014), but this can increase spu-

rious diapycnal mixing and extract too much energy from the resolved flow (Roberts and Marshall, 1998; Jansen and Held, 2014). Some attempts have been made to parameterize unresolved eddy mixing in eddy-resolving models using stochastic parameterizations (Manz and Zanna, 2014), additional equations in the model for subgrid kinetic energy and mixing length (Eden and Greatbatch, 2008; Jansen et al., 2015a), or switches that turn off parameterizations in regions where the largest mesoscale eddies are resolved (Hallberg, 2013) – all of which attempt to account for the spatial heterogeneity of mixing.

Large eddy simulation (LES) is an approach used to simulate turbulent flows in which the largest scales are resolved, but the smallest scales must be parameterized. Unlike coarse resolution approaches, LES uses the resolved flow to improve the subgrid closure. Subgrid closures in LES often rely on the presence of an ‘inertial cascade’ of a flow property, from large scales down to unresolved scales, by the turbulence (Kolmogorov, 1941; Kraichnan, 1967). In LES, ν and κ are chosen to provide damping that is consistent with an appropriate inertial cascade, while avoiding damping at scales above the grid scale (Smagorinsky, 1963; Leith, 1996). The values of ν and κ have an intrinsic dependence upon the local flow field and the grid resolution. For geophysical applications, LES is often used to simulate 3D turbulence, such as that in ocean boundary layers, using a traditional Smagorinsky subgrid scheme (Smagorinsky, 1963). The Smagorinsky subgrid scheme has been applied to ocean models (Griffies and Hallberg, 2000), but it extracts too much energy from the resolved flow (Jansen and Held, 2014) and much recent work has sought to provide backscatter or other stochastic schemes to re-inject energy into the resolved scales (Jansen et al., 2015b; Grooms et al., 2015; Zurita-Gotor et al., 2015). Mesoscale turbulence is not typical 3D turbulence because the effects of rotation and stratification confine the motions of mesoscale eddies to isopycnal surfaces. Recent work has developed and used LES techniques for 2D turbulence (Leith, 1996; Fox-Kemper and Menemenlis, 2008; Nadiga and Bouchet, 2011; Nguyen et al., 2011; San et al., 2011; 2013; Pietarila Graham and Ringler, 2013). Bachman et al. (2017) extended these ‘Leith’ or ‘mesoscale ocean large eddy simulation’ (MOLES) techniques to apply to the quasi-geostrophic (QG) turbulence regime in which mesoscale eddies reside. They found that idealised simulations of a frontal spin-down using a quasi-geostrophic extension of Leith (1996), or QG Leith, produced kinetic energy spectra which were more consistent with theory and exhibited less spectral roll-off at the grid-scale than simulations using a variety of other common mixing parameterizations. In addition, they showed that the 2D Leith and QG Leith schemes can be used to prescribe the GM-Redi parameters, so that the horizontal eddy momentum fluxes, and the along-isopycnal eddy tracer fluxes and tracer advection are parameterized consistently for the unresolved part of the mesoscale spectrum. Importantly, the amount of subgrid eddy tracer transport and restratification is not sufficient to fully replace that expected from unresolved eddies in the Bachman et al. (2017) scheme, but it is enough to regularize the tracer and density transport and provide consistent dissipation of potential vorticity by diffusion of buoyancy and viscosity.

In this paper we apply the 2D Leith and QG Leith parameterizations for eddy stresses and tracer transports within a global eddy-resolving ocean model, and compare the resultant simulations with those using a standard (biharmonic) subgrid scheme. The simulations, and the 2D Leith and QG Leith parameterizations, are described in Section 2. In Section 3, we compare these Leith simulations with simulations using a biharmonic mixing scheme. The results are discussed and summarized in Section 4.

2. Background and theory

2.1. Friction and diffusion parameterizations

The effects of subgrid processes in ocean models are often parameterized as frictional and diffusive forces acting on the velocity and tracer fields, respectively. For example, in the Parallel Ocean Program (POP) model, which shall be used in this study, the equations controlling the evolution of horizontal momentum and tracers (ϕ) are given by [Smith et al. \(2010\)](#),

$$\frac{\partial u}{\partial t} + A_u - fv = P_u + F_H(u) + F_V(u) \quad (1)$$

$$\frac{\partial v}{\partial t} + A_v + fu = P_v + F_H(v) + F_V(v) \quad (2)$$

$$\frac{\partial \phi}{\partial t} + A_\phi = D_H + D_V, \quad (3)$$

where A_α is the advection of α , f is the Coriolis parameter, u and v are the zonal and meridional velocity components respectively, and P_u and P_v are the pressure gradient forces in the zonal and meridional directions. The friction (F) and diffusion (D) operators are decomposed into horizontal and vertical components, denoted by subscripts H and V , respectively. The purposes of friction and diffusion in the model are to parameterize the effects of the subgrid scales and to provide numerical stability by damping noise at the grid scale. The vertical operators are parameterized as $F_V(\alpha) = \partial[\mu\partial\alpha/\partial z]/\partial z$, and $D_V = \partial[\mu_\phi\partial\phi/\partial z]/\partial z$, where μ and μ_ϕ are the vertical viscosity and vertical diffusivity respectively. The horizontal diffusion (D_H) is often adjusted to mix along isopycnal surfaces and an additional advective term is introduced to represent mesoscale eddy processes ([Gent and McWilliams, 1990](#)), in [Section 2.3](#) we discuss this in more detail.

The subgrid friction and diffusion parameterizations reduce the shear and the tracer gradients in the flow by mixing momentum and tracers, respectively, resulting in reduced velocity and tracer extrema. [Bachman et al. \(2017\)](#) showed how potential vorticity dissipation is related to these mixing processes. At the resolutions that are currently practical in global models, the diapycnal mixing needed to represent subgrid processes is much weaker than mixing along isopycnals, and this is approximated in models by parameterizing vertical/diapycnal mixing and horizontal/along-isopycnal mixing separately, with the former being relatively weak. In this paper we focus on the horizontal (i.e., approximately along-isopycnal in the biharmonic scheme, explicitly along-isopycnal in the GM-Redi approach) component of mixing, which at present resolutions is amenable to the Large Eddy Simulation approach. That is, it primarily represents the effects of the largest unresolved energy-containing features (which are small mesoscale eddies), using larger resolved eddies to inform the representation. Since the processes thought to generate diapycnal mixing occur on much smaller scales (e.g., breaking internal waves; [Jochum, 2009](#); [MacKinnon et al., 2013](#)), these processes are not yet sufficiently resolved for a Large Eddy Simulation approach and are therefore not altered in these experiments.

The most common parameterizations for the horizontal frictional force, F_H , and horizontal diffusion, D_H , are Laplacian,

$$F_H(u) = \nabla_h \cdot (\nu \nabla_h u), \quad D_H = \nabla_h \cdot (\kappa \nabla_h \phi), \quad (4)$$

or biharmonic,

$$F_H(u) = -\nabla_h^2(\nu_{bh} \nabla_h^2 u), \quad D_H = -\nabla_h^2(\kappa_{bh} \nabla_h^2 \phi), \quad (5)$$

operators. In these equations $\nabla_h = (\partial_x, \partial_y, 0)$ is the horizontal gradient operator, ν is the eddy viscosity and κ is the eddy diffusivity. The subscript $_{bh}$ denotes viscosity and diffusivity for

the biharmonic parameterization, which have different units than their Laplacian counterparts. The Laplacian mixing is analogous to molecular diffusion, and it is the leading order term in the Taylor series expansion of mixing. Biharmonic mixing is the second even-order (i.e., diffusive) term in the series expansion, and so its use as the leading order diffusion implies that the Laplacian term is zero ([Fox-Kemper and Menemenlis, 2008](#)). The biharmonic operator, despite being more complex to evaluate than the Laplacian, and requiring more boundary conditions, has the advantage of being more scale selective. This makes biharmonic horizontal mixing common in high-resolution ocean models, where it is not desirable for the parameterizations to damp the flow at scales larger than the grid ([Holland, 1978](#); [Griffies and Hallberg, 2000](#)). Note that horizontal tracer mixing, as in [Eqs. \(4\)](#) and [\(5\)](#), will cause diapycnal mixing in regions wherever isopycnals are not horizontal. A GM-Redi parameterization approach, which avoids spurious diapycnal tracer mixing in the equivalent of [Eq. \(4\)](#), will be described in [Section 2.3](#).

Regardless of whether a model uses a Laplacian or biharmonic operator, the viscosity and diffusivity magnitudes must still be chosen. This closure problem is often solved by using spatially and temporally constant viscosity (and diffusivity) values, which are then tuned to be large enough to prevent numerical instability everywhere in the domain, yet as small as possible, with additional corrections that may improve flow in specific regions (e.g. [Ezer and Mellor, 2000](#); [Chassignet and Garraffo, 2001](#); [Bryan et al., 2007](#); [Hecht et al., 2008](#)) or account for grid size variation in a non-uniform mesh. [Bachman et al. \(2017\)](#) showed that a carefully tuned harmonic or biharmonic model can perform well as a closure when the flow regime is relatively uniform. However, the physical purpose of the parameterization—to account for the mixing effects of subgrid eddies—requires the viscosity and diffusivity to represent the intensity of mixing by subgrid processes for any given tracer gradient or shear. The observed spatial and temporal variability in the strength and size of mesoscale eddies suggests that ν and κ (or ν_{bh} and κ_{bh}) should be spatially and temporally variable as well. Here, as in previous studies ([Leith, 1996](#); [Fox-Kemper and Menemenlis, 2008](#); [Nadiga and Bouchet, 2011](#); [Nguyen et al., 2011](#); [San et al., 2011, 2013](#); [Bachman et al., 2017](#)), this problem is addressed using LES techniques to develop a flow- and scale-adaptive viscosity and diffusivity.

2.2. Subgrid schemes: 2D Leith and QG Leith

In small-scale 3D turbulence, kinetic energy (KE) is transferred from the largest scales to the smallest scales, where it is dissipated by viscous effects, via an inertial cascade. KE dissipation, ε , occurs at wavenumber $k \approx \Lambda_s \varepsilon^{1/4} \nu^{-3/4}$, where Λ_s is a constant of order unity ([Kolmogorov, 1941](#)). If the resolution of a numerical simulation lies within the inertial cascade the viscosity can be increased until dissipation occurs at the grid scale, $k_* \approx 2\pi/\Delta_h$, where the asterisk indicates the smallest resolved scale following [Fox-Kemper and Menemenlis \(2008\)](#). Assuming local flow homogeneity, [Smagorinsky \(1963\)](#) found that the appropriate ‘Smagorinsky viscosity’ is,

$$\nu_s = (\Delta_h \Lambda_s / \pi)^2 \sqrt{S_{ij} S_{ij}}, \quad (6)$$

where $S_{ij} = (\partial u_i / \partial x_j + \partial u_j / \partial x_i) / 2$ is the rate-of-strain tensor. [Eq. \(6\)](#) is the basis of most 3D LES techniques. The diffusivity of tracers, κ , typically has a similar form to the viscosity. However, Smagorinsky-based LES schemes, such as the one above, are not designed for the turbulence in eddy-resolving global ocean models, where rotation and stratification break the assumed isotropic symmetries.

The majority of turbulent mixing in the interior of the ocean is driven by mesoscale eddies and occurs along isopycnal sur-

faces. The relatively small diapycnal component of mixing indicates that interior ocean turbulence is better approximated as a 2D or QG process, rather than a 3D process (e.g. Charney, 1971). Leith (1996) derived LES techniques appropriate for 2D turbulence, where the inertial subrange involves a downscale cascade of enstrophy rather than KE. In this case, the wavenumber at which enstrophy dissipation, η , occurs is given by $k \approx \Lambda_{2d}\eta^{1/6}v^{-1/2}$. Fox-Kemper and Menemenlis (2008) demonstrated that enstrophy dissipation at the gridscale can be achieved by scaling the eddy viscosity such that

$$\nu_{2d} = \left(\frac{\Delta_h \Lambda_{2d}}{\pi} \right)^3 |\nabla_h q_{2d}|, \quad (7)$$

where $q_{2d} = \nabla_h \times \mathbf{u}$ is the vertical vorticity. Fox-Kemper and Menemenlis (2008) noted that a viscosity which depends only on the flow through the vertical vorticity is unstable to divergent motion. They suggest refining Eq. (7) to include a term proportional to the gradient of horizontal divergence, which is only a small correction for rapidly rotating mesoscale flows,

$$\nu_{2d} = \left(\frac{\Delta_h \Lambda_{2d}}{\pi} \right)^3 \sqrt{|\nabla_h q_{2d}|^2 + |\nabla_h(\nabla_h \cdot \mathbf{u})|^2}. \quad (8)$$

Eq. (8) will be referred to as the 2D Leith subgrid scheme.

Bachman et al. (2017) extend the 2D Leith subgrid scheme to include the effects of stratification and planetary rotation through the quasi-geostrophic (QG) approximation. The QG approximation is appropriate for mesoscale flows, where the Rossby number is less than unity but the flow is affected by local variations in stratification. They propose the QG Leith parameterization,

$$\nu_{qg} = \left(\frac{\Delta_h \Lambda_{qg}}{\pi} \right)^3 \sqrt{|\nabla_h q_{qg}|^2 + |\nabla_h(\nabla_h \cdot \mathbf{u})|^2}, \quad (9)$$

where $\nabla_h q_{qg} = [\nabla_h q_{2d} + \nabla_h f + \partial(f[\nabla_h b']/N^2)/\partial z]$ is the horizontal gradient of the QG potential vorticity, f is the Coriolis parameter, b' is the buoyancy perturbation (∇_h eliminates the ambient stratification contribution; Appendix A), and N is the buoyancy frequency of the vertical stratification. The term containing vertical derivatives is the QG vortex stretching. We have included a planetary vorticity term in Eq. (9), which can be simplified by noting that $\nabla_h f = (0, \beta)$, where β is the local rate of change of f with meridional displacement.

The non-dimensional parameters Λ_{2d} and Λ_{qg} in the 2D Leith and QG Leith schemes should be order unity. Bachman et al. (2017) compared two choices of Λ_{2d} and Λ_{qg} in an idealized ocean model; using constant values, and using a dynamic filter to optimize these parameters. The dynamic filter was more computationally expensive, but provided no significant benefits, compared to using constant parameters. As a result we use constant values in the following simulations with $\Lambda_{2d} = \Lambda_{qg} = 1$. For future guidance, these parameters may be varied somewhat to accommodate, for example, different amounts of noise resulting from different numerical schemes. However, regional tuning or large changes to these parameters are not supported by the underlying theory.

The 2D Leith and QG Leith closures are designed to dissipate momentum at rates appropriate for the inertial cascades of kinetic energy ($\mathbf{u} \cdot \mathbf{u}/2$; Eq. (6)), enstrophy ($q_{2d}^2/2$; Eq. (8)), and QG potential enstrophy ($q_{qg}^2/2$; Eq. (9)). The latter is the most applicable to the mesoscale eddy range, in which the grid scale of high-resolution ocean models currently resides. Bachman et al. (2017) showed that using QG Leith in a mesoscale resolving idealized ocean model improved energy and potential enstrophy spectra down to the grid scale when compared to other subgrid schemes. The aim of the present work is to investigate how using QG Leith and 2D Leith subgrid schemes affects ocean properties within an

eddy-resolving global ocean model. Bachman et al. (2017) showed that QG Leith and 2D Leith are also numerically stable in simulations which do not resolve the potential enstrophy cascade, although numerical stability does not guarantee accuracy at coarser resolutions.

2.3. Tracer diffusivity in 2D and QG Leith

The diffusivities in QG Leith and 2D Leith are calculated in a manner identical to the viscosity. However, there are two important differences between the full diffusion and friction operators. First, the parameterization of diffusion is modified to mix along isopycnals rather than in the horizontal, to avoid the diapycnal tracer mixing caused by Eq. (4) in regions of sloping isopycnals (Redi, 1982). Second, the Gent-McWilliams (GM) bolus velocity is included, which extracts potential energy from sloped isopycnals (Gent and McWilliams, 1990; Griffies, 1998) and is critical for adiabatic subgrid tracer transport to affect potential enstrophy (Bachman et al., 2017).

The resulting along-isopycnal diffusion operator in 2D Leith and QG Leith is given by

$$D_H = \nabla_3 \cdot ([\mathbf{K} + \mathbf{B}] \cdot \nabla_3 \phi), \quad (10)$$

where $\nabla_3 = (\partial_x, \partial_y, \partial_z)$ is the full (3D) gradient operator. \mathbf{K} is the (small-slope) Redi diffusion tensor given by,

$$\mathbf{K} = \kappa_i \begin{pmatrix} 1 & 0 & -\rho_x/\rho_z \\ 0 & 1 & -\rho_y/\rho_z \\ -\rho_x/\rho_z & -\rho_y/\rho_z & (\rho_x^2 + \rho_y^2)/\rho_z^2 \end{pmatrix}, \quad (11)$$

κ_i is the isopycnal diffusivity and $\rho_k = \partial \rho / \partial k$ is the density gradient. \mathbf{B} is the GM antisymmetric tensor (Griffies, 1998),

$$\mathbf{B} = \mu_{gm} \begin{pmatrix} 0 & 0 & \rho_x/\rho_z \\ 0 & 0 & \rho_y/\rho_z \\ -\rho_x/\rho_z & -\rho_y/\rho_z & 0 \end{pmatrix}, \quad (12)$$

where μ_{gm} is the buoyancy diffusivity. \mathbf{B} represents the advective effects of eddies as they extract baroclinic potential energy stored in sloped isopycnals. The density-dependent terms in \mathbf{K} and \mathbf{B} are related to the slope of the isopycnal surface, which is assumed to be small. It is easily verified that $\nabla_3 \rho \cdot \mathbf{K} \cdot \nabla_3 \rho = \nabla_3 \rho \cdot \mathbf{B} \cdot \nabla_3 \rho = 0$, indicating that the density fluxes are indeed along-isopycnals. Similarly, $\nabla_3 \rho \cdot \mathbf{K} \cdot \nabla_3 \tau = 0$, indicating that tracer diffusion is along isopycnals, while tracer advection from $\mathbf{B} \cdot \nabla_3 \tau$ is not generally along isopycnals. These fluxes are used to replace the horizontal mixing D_H in (3). Despite their small vertical component required to flux along isopycnals, we refer to them with the simpler forms in (3) collectively as horizontal.

The total transport tensor is then,

$$\mathbf{K} + \mathbf{B} = \begin{pmatrix} \kappa_i & 0 & -(\kappa_i - \mu_{gm})\rho_x/\rho_z \\ 0 & \kappa_i & -(\kappa_i - \mu_{gm})\rho_y/\rho_z \\ -(\kappa_i + \mu_{gm})\rho_x/\rho_z & -(\kappa_i + \mu_{gm})\rho_y/\rho_z & \kappa_i(\rho_x^2 + \rho_y^2)/\rho_z^2 \end{pmatrix}. \quad (13)$$

The GM bolus velocity (μ_{gm}) is commonly used only in simulations which do not resolve mesoscale eddies. However, Bachman et al. (2017) demonstrated that the bolus velocity is required in high-resolution simulations to account for the buoyancy budget contribution to PV dissipation, and to ensure a positive-definite sink of PV. Furthermore, they found that the optimal choice of bolus velocity was $\mu_{gm} = v$. In the context of coarse numerical models, Dukowicz and Smith (1997) suggest that $\kappa_i \approx \mu_{gm}$, while

Smith and Marshall (2009) and Abernathey et al. (2013) recommend a distinction between μ_{gm} and κ_i when κ_i varies in the vertical. Bachman et al. (2017) note that either form may be calculated consistently from v in the QG Leith framework. Here we assume that the coarse model results can be applied when the mesoscale eddy field is partially resolved and we choose the simpler option of $v = \kappa_i = \mu_{gm}$. This choice results in the closest approximation—considering the form of the operators in (13)—to the expected dissipation of potential enstrophy and consistent potential vorticity fluxes (Bachman et al., 2017). These operators combine horizontal diffusion with vertical diffusive and advective tracer transport to produce fluxes oriented along isopycnals.

2.4. Model description

This study uses the POP model at nominal 0.1° horizontal resolution described in Maltrud and McClean (2005). The simulations use a tripole grid, with a standard Mercator grid in the Southern hemisphere and two northern poles centered over land in Asia and North America. The simulations use a repeating synthetic year of forcing data provided by the Coordinated Ocean-Ice Reference Experiments (CORE, Large and Yeager, 2009) and partial bottom cells to represent bottom topography. There are 62 vertical levels which increase in separation with depth, from 10 m vertical resolution at the surface to 250 m resolution in the abyssal ocean. The details of this POP forcing are described in Bryan and Bachman (2015). The vertical viscosity (μ) and vertical diffusivity are parameterized using the KPP scheme (Large et al., 1994; Smith et al., 2010) and have background abyssal values ($5.5 \times 10^{-5} \text{ m}^2 \text{ s}^{-1}$) representing internal wave mixing (MacKinnon et al., 2013). For simplicity, these simulations do not use a submesoscale parameterization scheme (Fox-Kemper et al., 2011) or variable abyssal vertical diffusivity (Jochum, 2009).

This study presents three simulations which differ only in their horizontal mixing parameterizations (F_H and D_H in Eq. (3)). The first simulation uses a biharmonic horizontal mixing operator for tracers and momentum (Eq. (5)). The biharmonic viscosity and diffusivity vary with the horizontal area of the grid cell, A , such that they scale with $A^{3/2}$ (Maltrud and McClean, 2005). This scaling differs from the choice of $\nu_{bh} \propto A$ used by Bachman et al. (2017). The grid area is a maximum at the equator where the viscosity is $2.7 \times 10^{10} \text{ m}^4 \text{ s}^{-1}$ and the diffusivity is $3 \times 10^9 \text{ m}^4 \text{ s}^{-1}$. The second simulation uses the ‘2D Leith’ viscosity (Eq. (8) with $\Lambda_{2d} = 1$) within a horizontal Laplacian friction scheme (Eq. (4)). The third simulation uses the ‘QG Leith’ viscosity (Eq. (9) with $\Lambda_{qg} = 1$) within a horizontal Laplacian friction scheme. The viscosity calculations in the Leith schemes are detailed in Appendix A. One important detail is that the QG Leith scheme transitions to the 2D Leith scheme within the boundary layer by neglecting the stretching term in (9), as the stratification is too low there to expect quasigeostrophic dynamics to apply. Both Leith simulations use the GM-Redi tracer diffusion, and the isopycnal and thickness diffusivities are set equal to the viscosity following Bachman et al. (2017). The biharmonic simulation applies biharmonic horizontal diffusion, rather than the GM-Redi harmonic diffusion used in the 2D Leith and QG Leith simulations.

Simulations are spun-up for 15 years using the biharmonic scheme, after which the appropriate subgrid scheme is introduced and the simulations are continued for 5 years. The global integral of kinetic energy within the 2D and QG Leith simulations (not shown) stabilizes within a year of the switch in subgrid schemes. As a result, we assume that in the final four years the barotropic component of the simulations has spun-up, and so we can analyze the dynamical differences between simulations. The data shown in the subsequent figures use either monthly mean averages over the final four years of the simulations or, where instantaneous snap-

shots are required, the flow field taken on the first timestep of January in the second year of the simulation. The stratification of the ocean requires decades to equilibrate, and so we do not investigate the available potential energy cycle or baroclinic features here.

In POP, the horizontal friction and diffusion operators contain several vector calculus operations. This results in a combination of physical operations, which are designed to represent the physics of the processes which are being parameterized, and metric terms, which result from the non-Cartesian grid used in the global model (Williams, 1972; Wajsowicz, 1993). In the following sections we focus our discussion on the physical justification of different subgrid schemes, and so we will neglect the metric terms – but note that metric terms are included in the POP code implementation.

3. Results

3.1. Viscosity fields

The choice of subgrid scheme controls the viscosity and diffusivities within the model. Fig. 1 (top) shows the viscosity at a depth of 100 m for the 2D Leith simulation. There is significant spatial variation in the viscosity. The Gulf Stream and Kurushio have viscosities which exceed those in parts of the Southern or Arctic Ocean by two orders of magnitude. The largest viscosities are near $100 \text{ m}^2 \text{ s}^{-1}$, while the smallest viscosities are less than $1 \text{ m}^2 \text{ s}^{-1}$.

There are significant differences between the viscosity of the QG Leith and 2D Leith schemes. The viscosity is greater in QG Leith than in 2D Leith, and the greatest increases in viscosity are in the Southern Ocean, particularly near the Antarctic Circumpolar Current (ACC), in the North Pacific and North Atlantic basins, and in the Western Boundary Currents (WBCs). Both QG Leith and 2D Leith have similar viscosities near the equator where f , and hence the stretching term in Eq. (9), is small but $\beta = \partial f / \partial y$ is at its maximum, indicating that β does not contribute significantly to viscosity, consistent with Bachman et al. (2017). Indeed, β alone leads to only an $O(1) \text{ m}^2 \text{ s}^{-1}$ effect. QG stretching processes, which could cause the significant changes in viscosity between the QG Leith and 2D Leith schemes, include convective mixing in the Northern (winter) hemisphere driving weak stratification (small N^2). There are some regions in the North Atlantic and Greenland Sea which have similar viscosities in both 2D Leith and QG Leith simulations, which are co-located with areas of mixed layer depths greater than 100 m (not shown). The maps in Fig. 1 are plotted at 100 m depth because this is where QG Leith and 2D Leith viscosities differ the most (see discussion of Fig. 2).

In contrast to the 2D Leith and QG Leith schemes, the biharmonic viscosity (not shown) varies only with the horizontal area of the grid. At high latitudes the grid becomes smaller, and the biharmonic viscosity decreases. The biharmonic viscosity reduces by less than an order of magnitude between the equator and 50°N/S, a smaller change than is seen for the Leith viscosities. The Leith viscosities are aware of both the model grid and the local ocean properties. It is clear that there is not a monotonic decrease in Leith viscosities from Equator to pole, and so the Leith viscosities are dominated by changes in the ocean dynamics, rather than changes in the grid, across most of the ocean.

The magnitude of viscosity in the biharmonic subgrid scheme can be converted to an ‘equivalent Laplacian viscosity’ ($\nu_{eq} = -8\nu_{bh}/A$; Griffies and Hallberg, 2000; Fox-Kemper and Menemenlis, 2008), which allows a more direct comparison with the 2D Leith and QG Leith schemes. In the biharmonic simulation, ν_{eq} is between 365 and $1750 \text{ m}^2 \text{ s}^{-1}$ everywhere in the ocean. These values are 1–2 orders of magnitude larger than the typical viscosities of the 2D Leith and QG Leith simulations (Figs. 1 and 2). This es-

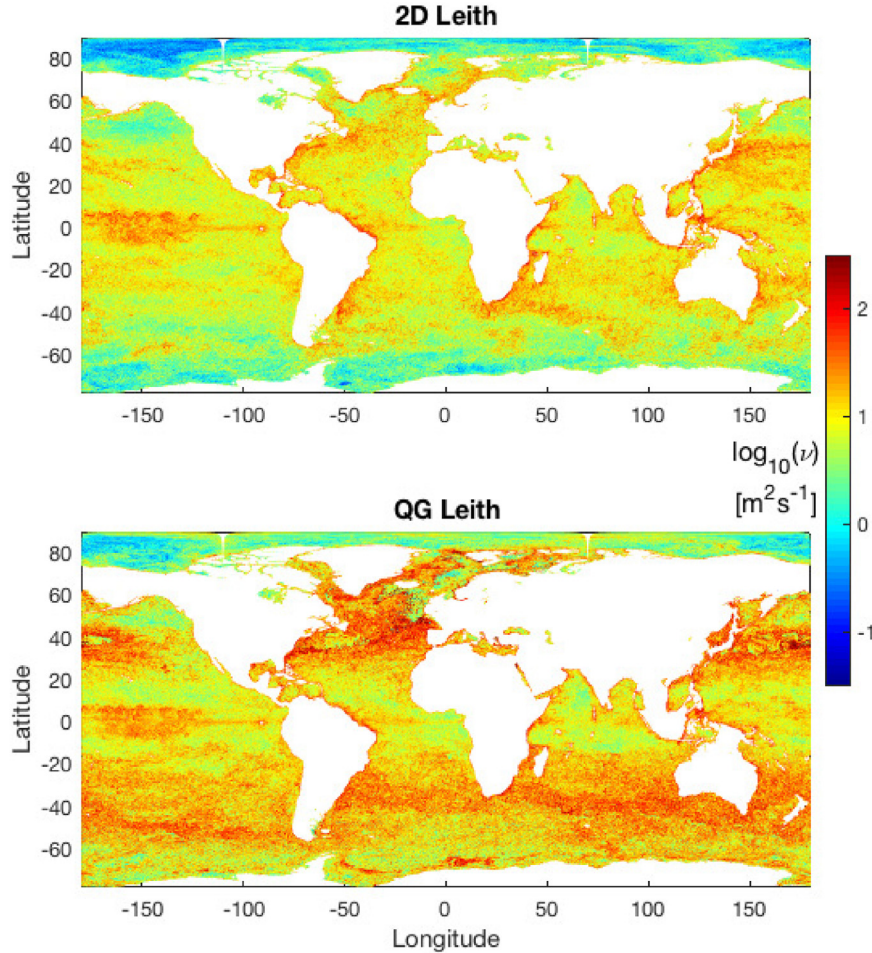


Fig. 1. Global maps of viscosity at 100 m depth for the 2D Leith (top) and QG Leith (bottom) subgrid schemes. The color scale is logarithmic, and the latitude axis ranges from 78°S to 90°N. This figure uses an instantaneous snapshot of the flow field. (For interpretation of the references to color in this figure legend, the reader is referred to the web version of this article.)

timate portends that the biharmonic scheme will damp ocean dynamics significantly more than the 2D Leith and QG Leith schemes.

The Leith viscosities also differ from the biharmonic viscosity because they vary with depth. Fig. 2 shows the global median viscosity as a function of depth from the 2D Leith and QG Leith simulations. The viscosity is large in the upper kilometer, and drops off in the ocean interior, before increasing again near the ocean bottom. The QG Leith viscosity is greater than the 2D Leith viscosity, most noticeably between 100 m and 1 km depth. This is consistent with mesoscale eddies, and their associated buoyancy perturbations, being present in the thermocline. At depths shallower than 100 m, the QG Leith viscosity is reduced because the stretching term is ignored within the boundary layer (following Bachman et al., 2017). Near the surface the GM-Redi parameterization also uses a tapering scheme (Ferrari et al., 2008). In the interior of the ocean QG Leith modestly increases the median and upper-quartile of viscosity relative to 2D Leith, while leaving the lowest viscosity regions unaffected.

3.2. Kinetic energy

The subgrid schemes differ in their damping of momentum anomalies, and will therefore differ in impact on kinetic energy. Fig. 3 shows a snapshot of the global kinetic energy field at the surface for the biharmonic and 2D Leith simulations. The kinetic energy varies by several orders of magnitude spatially, and is largest near the equator, in the ACC, and in WBCs. It is difficult

to distinguish significant differences between the global maps of kinetic energy for the two simulations. The global surface kinetic energy map for the QG Leith simulation (not shown) is similar to the other simulations.

While the global surface KE maps are similar, differences in surface KE between simulations become apparent if we look at a regional scale. Fig. 3 also shows the surface kinetic energy zoomed in on a region of the South Pacific. The maximum magnitude of kinetic energy in this region is similar across all simulations, but the spatial scales at which the energetic features are present varies with the subgrid scheme. In this region the 2D Leith simulation has energetic features at a range of scales, spanning several tenths of a degree to several degrees, and the biharmonic simulation has fewer small scale energetic features. The biharmonic kinetic energy field looks, in some respects, like a spatially smoothed version of the 2D Leith kinetic energy field. Biharmonic schemes are often assumed to remove energy at smaller scales than Laplacian schemes (Griffies and Hallberg, 2000), but the use of 2D Leith viscosity with a Laplacian operator allows more energy in small scale features than the biharmonic scheme. The QG Leith simulation has smaller energetic features than the biharmonic scheme, but less of these features than the 2D Leith simulation. It should be noted that some of these differences could be due to the chaotic nature of the turbulent flow field, and differences in large-scale advection.

Fig. 4 shows the climatologies of eddy kinetic energy (EKE) as a function of both latitude and depth for each simulation. The

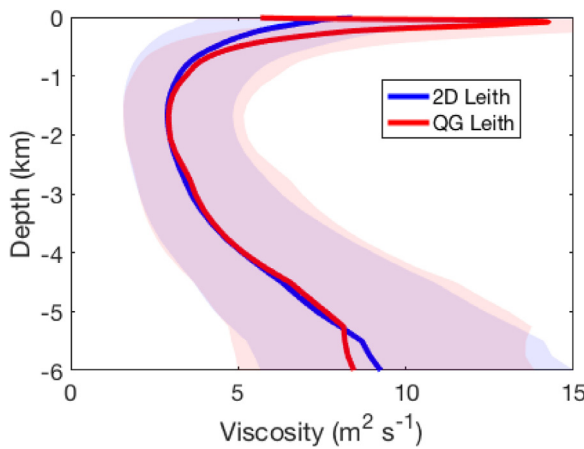


Fig. 2. Depth profiles of globally averaged viscosity. Lines show the global median viscosity for the 2D Leith and QG Leith schemes. Shading shows the inter-quartile range of each viscosity profile. The median is shown rather than the mean because the latter is dominated by the largest viscosities (note Fig. 1 has a log color scale). The equivalent Laplacian viscosity in the biharmonic simulation is between 365 and 1750 $\text{m}^2 \text{s}^{-1}$ everywhere (Griffies and Hallberg, 2000). This figure uses an instantaneous snapshot of the flow field. (For interpretation of the references to color in this figure legend, the reader is referred to the web version of this article.)

surface EKE is similar across all the simulations, and shows good agreement with drifter observations (Lumpkin and Johnson, 2013) at mid- to high-latitudes but lower than observed EKE levels in the extra-tropics. At 3379m depth the 2D and QG Leith simulations have more EKE and MKE than the biharmonic simulation at most latitudes. In the Southern Ocean the Leith simulations have almost 50% more EKE than the biharmonic simulation, while in the weakly energetic extra-tropics they have almost 100% more EKE.

The depth profiles show similar EKE levels across all simulations in the upper 500m of the ocean, with slightly more energy in the 2D Leith simulation. Below 1km the 2D and QG Leith simulations have 50% more EKE than the biharmonic simulation. The effect that this difference has on the energy pathways within the Global Ocean will be discussed in Section 3.4. The mean kinetic energy (MKE) is lower than the EKE but shows similar variation with depth, and the Leith simulations have almost 100% more MKE than the biharmonic simulation at depths below 3km. It should be noted that the variations in EKE and MKE depth profiles across simulations are a result of the differing viscosity magnitudes and the Leith simulations having a depth-dependent viscosity (Fig. 2).

The differences between the kinetic energy within the 2D Leith and QG Leith simulations can be interpreted physically. The 2D Leith and QG Leith schemes produce similar viscosities below the thermocline ($|z| > 1 \text{ km}$), where the stratification is weaker, suggesting that the quasi-geostrophic stretching is small relative to the vorticity below the pycnocline, where motion is dominated by low vertical modes with limited vertical shear and horizontal buoyancy variance. Moving upwards into the thermocline, quasi-geostrophic processes become more important; horizontal buoyancy gradients are stronger and mesoscale eddies are ubiquitous. This causes the stretching component of the QG Leith scheme (Eq. (9)) to increase the viscosity (Fig. 2), and as a result reduce the kinetic energy, relative to the 2D Leith scheme. At the surface the viscosity of the QG Leith scheme does not include a stretching component, because the surface is always within the boundary layer. However, the reduced kinetic energy of the thermocline and the presence of vertical momentum diffusion (F_V in Eq. (3)), when combined, increase interior drag on the surface and result in slightly smaller surface kinetic energy in the QG Leith simulation relative to the 2D Leith simulation.

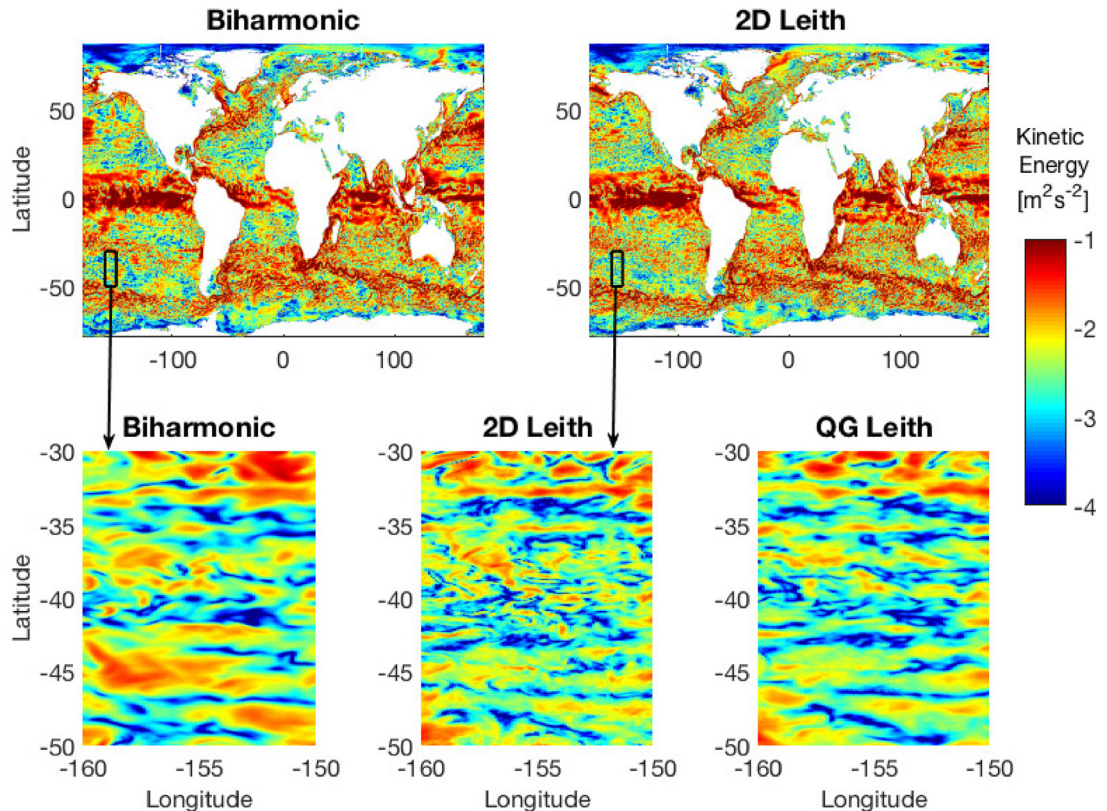


Fig. 3. Snapshots of surface kinetic energy for each simulation. Shown are the global maps (top) and regional maps (bottom) for the region indicated by the black rectangle on the global maps. Note that the colorscale is logarithmic. The global map for the QG Leith simulation is not shown, but is quantitatively similar to the 2D Leith global map. (For interpretation of the references to color in this figure legend, the reader is referred to the web version of this article.)

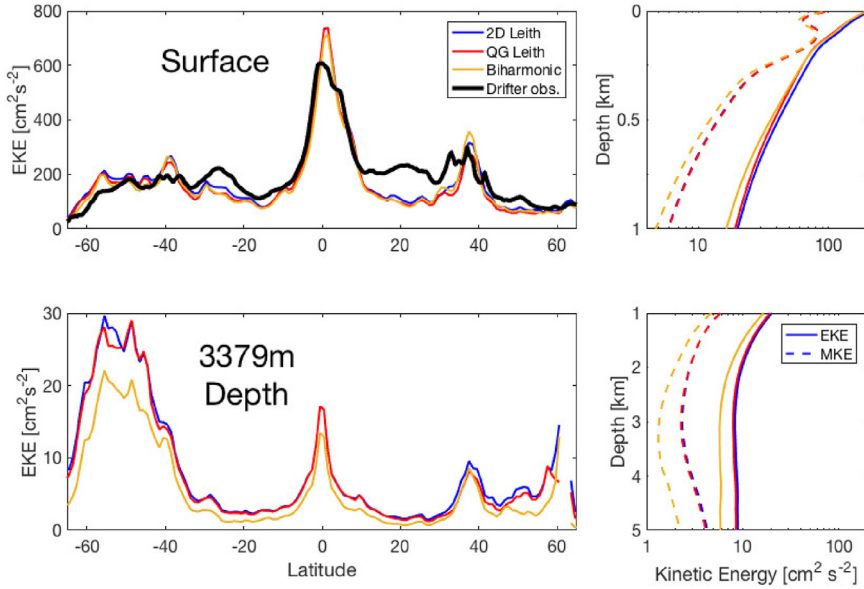


Fig. 4. Climatology of eddy kinetic energy (EKE) as a function of (left) latitude and (right) depth from each simulation. The latitudinal variation of EKE is shown at the surface (top) and at a depth of 3379 m depth (bottom). The black line shows the surface EKE measured by Lumpkin and Johnson (2013) using drifters. The depth profiles of EKE are stretched near the surface to emphasize their differences. Also shown are the depth profiles of mean kinetic energy (MKE). The climatology is calculated from the final 4 years of each simulation. (For interpretation of the references to color in this figure legend, the reader is referred to the web version of this article.)

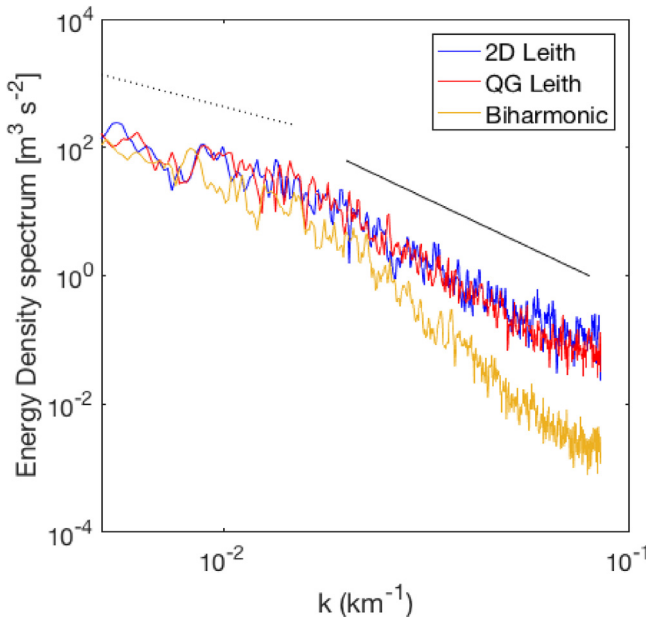


Fig. 5. Energy density spectrum for kinetic energy along a zonal transect (58°S) at 900 m depth in the ACC. The spectrum is smoothed using Welch's method (Welch, 1967). Also shown are reference spectral slopes with gradients of -3 (solid line) and $-5/3$ (dotted line), expected for the QG potential enstrophy cascade and the inverse kinetic energy cascade respectively. This figure is analogous to Fig. 3 of Jochum et al. (2008), but in a model with a roughly ten times finer grid. (For interpretation of the references to color in this figure legend, the reader is referred to the web version of this article.)

The effect of the subgrid scheme on the spatial scale of energetic features is also readily seen in Fig. 5, which shows the spectral density of kinetic energy at 900 m depth for a zonal transect around the Southern Ocean. The three simulations have similar energy at the largest scales, and the spectral slopes at scales larger than 100 km are consistent with the inverse cascade of energy typical of QG turbulence above the first baroclinic Rossby deformation radius (Smith et al., 2002). At spatial scales less than 100 km, the spectra diverge across the simulations. The QG Leith and 2D Leith

simulations have spectral slopes similar to the -3 slope expected for the QG enstrophy cascade below the baroclinic deformation radius. In contrast, the biharmonic simulation has a steeper slope than expected from theory, and has more than an order of magnitude less energy at the smallest scales than the 2D Leith and QG Leith simulations. The differences are not only present at the smallest scale, but persist to scales 5–10 gridpoints in dimension. These differences are despite the fact that the biharmonic viscosity is chosen to be scale selective and dissipate primarily at small scales. The kinetic energy spectra imply that the 2D Leith and QG Leith schemes do not cause excessive damping of the resolved flow, increasing the fidelity of energetic features at and below the deformation radius relative to biharmonic schemes. Near the grid scale there is more energy in the 2D Leith simulation than in the QG Leith simulation, although this difference is small.

Recent discussions (e.g., Capet et al., 2008; Le Traon et al., 2008; Cole and Rudnick, 2012; Timmermans et al., 2012; Callies and Ferrari, 2013) have centered on whether observed spectra match a k^{-3} slope consistent with a QG potential enstrophy cascade or 2D enstrophy cascade—and therefore consistent with the QG Leith or 2D Leith closures—or a shallower slope consistent with various submesoscale dynamical regimes (frontal, surface quasi-geostrophy, lack of a cascade, etc.) or an internal wave spectrum. In regions or depths where there is an active mesoscale or weak submesoscale and internal waves, the observed slopes tend toward k^{-3} . In regions where submesoscale phenomena or internal waves are strong, shallower slopes are observed. In these submesoscale or wavy regions, the Leith closures are improper, but these simulations and Bachman et al. (2017) show that they remain stable and numerically robust, if somewhat inaccurate. None of the observations show slopes steeper than a k^{-3} slope, as exhibited by the biharmonic scheme result in Fig. 5.

In a coupled atmosphere-ocean general circulation model the differences between mesoscale dynamics under different subgrid schemes could impact atmosphere-ocean coupling. Previous studies have shown that coupling between mesoscale eddies and the atmosphere can change atmospheric winds (Small et al., 2008; Chelton and Xie, 2010), large-scale ocean circulation (Hogg et al., 2009), and ocean-atmosphere fluxes (Frenger

et al., 2013; Byrne et al., 2016). In addition, resolving mesoscale eddies can affect the ocean response to changes in atmospheric forcing (Munday et al., 2013). These effects cannot be studied using the present ocean-only numerical simulations, but they could provide a further source of sensitivity to subgrid friction parameterizations in coupled atmosphere-ocean models.

3.3. Horizontal viscous dissipation of kinetic energy

The variation of kinetic energy between models demonstrates that the choice of subgrid scheme affects the energetics of the flow. The kinetic energy budget of ocean models has a number of important terms. Kinetic energy is supplied to the ocean through the surface wind stress and baroclinic potential energy extraction. The removal of kinetic energy from the ocean is predominantly through horizontal and vertical friction, and bottom drag. In the following section we diagnose how changes in the horizontal friction operator affect the balance between different sinks of kinetic energy across our simulations.

The effects of the horizontal friction operator on kinetic energy can be calculated directly from the model equations. Taking the inner product of the horizontal velocities and their tendency equations (Eq. (3)) to produce the kinetic energy equation, we find that the effect of friction in the Leith schemes is given by (shown here for the x -component of velocity),

$$u[\nabla_h \cdot (\nu \nabla_h u)] = \nabla_h \cdot [\nu \nabla_h (u^2/2)] - \nu (\nabla_h u) \cdot (\nabla_h u). \quad (14)$$

The first term on the right hand side of the equation represents the diffusion of energy due to friction and vanishes upon volume integration with suitable viscous boundary conditions. The second term on the right hand side is always negative and represents the dissipation of kinetic energy. The metric terms have been neglected for clarity. The equivalent of Eq. (14) for the biharmonic scheme is,

$$\begin{aligned} -u[\nabla_h^2(\nu_{bh} \nabla_h^2 u)] &= \nabla_h \cdot [\nu_{bh}(\nabla_h^2 u) \nabla_h u - u \nabla_h(\nu_{bh} \nabla_h^2 u)] \\ &\quad - \nu_{bh}[\nabla_h^2 u]^2, \end{aligned} \quad (15)$$

where the last term on the right is always negative for $\nu_{bh} > 0$. In contrast to Eq. (14), the divergence term in (15) does not necessarily integrate globally to zero, but the global integral is small relative to that of the positive definite term in POP. For the divergence term in Eq. (15) to integrate to zero would require higher-order boundary conditions, which would be there only because of the higher-order derivatives in a biharmonic scheme. We will not investigate the divergence term further.

The dissipation, ε , is defined as the sign-definite term in Eqs. (14) and (15), summed over both the horizontal velocity components. This term always results in a sink of kinetic energy at both local and globally integrated scales. The dissipation is given by,

$$\varepsilon = \nu[(\nabla_h u) \cdot (\nabla_h u) + (\nabla_h v) \cdot (\nabla_h v)] \quad (16)$$

$$\varepsilon = \nu_{bh}[(\nabla_h^2 u)^2 + (\nabla_h^2 v)^2], \quad (17)$$

for the harmonic Leith and biharmonic schemes respectively. Following convention, the dissipation is defined as positive.

Fig. 6 shows the global maps and probability distribution functions (PDF) of logarithmic dissipation at 100 m depth for each simulation. The global distribution of dissipation follows a log-normal distribution for all subgrid schemes. This indicates that dissipation is not evenly spread across regions, but instead the majority of the dissipation occurs at a small fraction of locations. Such a dissipation distribution is commonly understood to occur in finescale turbulence under molecular viscosity (Yaglom, 1966; Pope and Chen, 1990), but here the dissipation is that of mesoscale turbulence by

subgrid schemes. This could be an important property to consider, for example, when choosing how and where to re-inject kinetic energy in backscatter schemes.

The biharmonic simulation has more dissipation than the Leith simulations. This is because the viscosities in the 2D Leith and QG Leith simulations are smaller than the equivalent Laplacian viscosity of the biharmonic simulation ($\nu \ll \nu_{bh}/(8A)$; Fig. 1), which is partially due to the flow-awareness of the Leith schemes allowing smaller viscosity values to remain numerically stable. The differences between the Leith simulations are relatively small but the QG Leith simulation has slightly more dissipation than the 2D Leith simulation, because the inclusion of QG stretching increases the viscosity (Fig. 2).

The spatial distribution of dissipation at 100 m depth differs across the simulations. Most of the dissipation at this depth occurs in the Southern Ocean, near WBCs, and at the Equator in all simulations. However, the strong dissipation is confined to smaller regions in the QG Leith and 2D Leith simulations relative to the biharmonic simulation, demonstrating that the biharmonic subgrid scheme is less scale-selective than the flow-aware 2D Leith and QG Leith schemes. In quiescent regions away from strong currents the biharmonic simulation has greater dissipation than the Leith simulations. The regions of high dissipation in all simulations are approximately co-located with the regions of high viscosity in the QG Leith simulation (Fig. 1). Since some of these high dissipation regions, such as the ACC, do not have large ν in the 2D Leith simulation, the similarity of the dissipation maps suggests that the flow field is an important factor affecting dissipation.

Because all the simulations have reached an equilibrium with respect to their global kinetic energy (not shown), the differences in kinetic energy dissipation between the simulations suggests that there are differences in the global kinetic energy budget between the simulations.

3.4. Other sinks of kinetic energy

Changing the subgrid scheme for horizontal viscosity affects the distribution of kinetic energy and its dissipation, but horizontal friction is not the only sink of kinetic energy in POP. The friction operators in Eq. (3) are also affected by boundary conditions, namely wind stress and bottom drag, and by vertical friction, as detailed in Appendix B. Bottom drag always acts as a sink of momentum and kinetic energy at the deepest ocean gridpoints. Vertical friction has a similar form to the Laplacian horizontal friction, and it acts as both a sink of kinetic energy (analogous to Eq. (16)) and diffusion of kinetic energy.

Fig. 7 plots the PDFs of the depth-integrated kinetic energy loss through horizontal friction (dissipation), bottom drag, and vertical friction. The depth-integration allows us to look at the total energy being dissipated in a given region. Like the dissipation at 100 m, the depth-integrated dissipation follows a roughly log-normal distribution and is smaller in the 2D Leith and QG Leith simulations than in the biharmonic simulation. The bottom drag in the 2D Leith and QG Leith simulations is much larger than in the biharmonic simulation. The bottom drag depends only on the magnitude of the bottom velocity, and so the PDFs are consistent with the Leith simulations having 50% more kinetic energy in the deep ocean than the biharmonic simulation (Fig. 3). The vertical friction term shows little variation between the simulations.

Fig. 8 shows global maps of the kinetic energy sinks, integrated over the depth of the water column, for the biharmonic and QG Leith simulations (2D Leith results in figures which are similar to QG Leith). As suggested by the depth-integrated dissipation PDFs, most of the dissipation occurs in a small number of regions and these correlate with regions of large viscosity in the QG Leith simulation. The dissipation in the biharmonic simulation is stronger

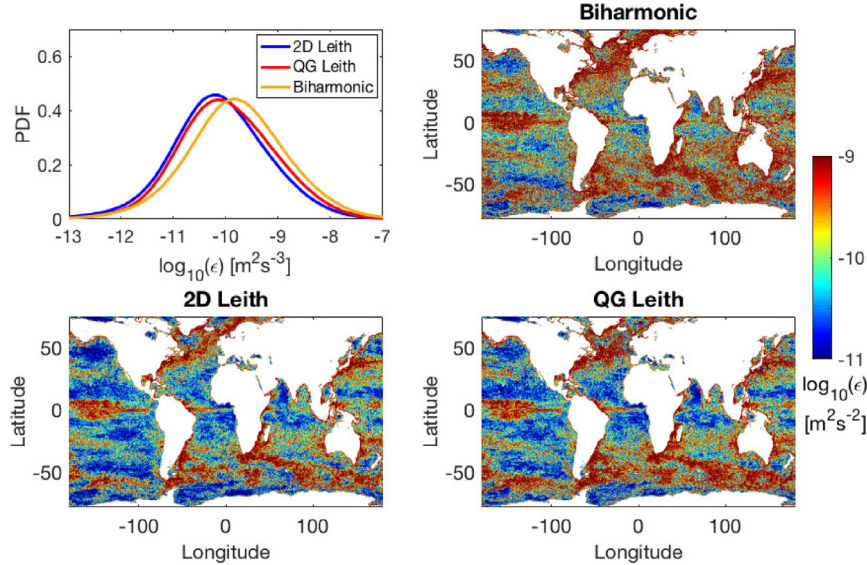


Fig. 6. Dissipation of kinetic energy at a depth of 100m in each simulation. Shown are the PDF of $\log_{10}(\epsilon)$ for different subgrid schemes (top left), and the global maps of dissipation for the Biharmonic (top right), 2D Leith (bottom left) and QG Leith (bottom right) simulations. Note the logarithmic color scale. This figure uses an instantaneous snapshot of the flow field. (For interpretation of the references to color in this figure legend, the reader is referred to the web version of this article.)

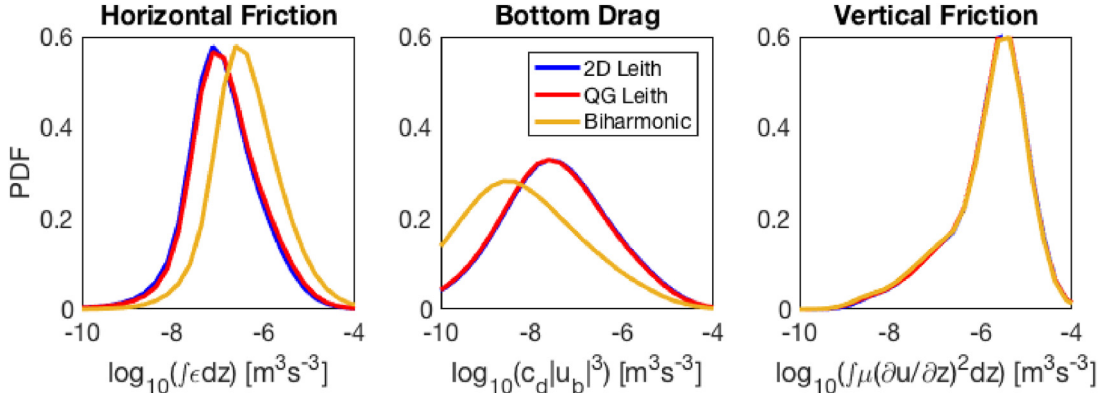


Fig. 7. PDFs of each depth-integrated frictional sink of kinetic energy in different simulations. Shown are the (a) dissipation [horizontal friction], (b) bottom drag, and (c) vertical friction sink of KE. Note that the *logarithm* of the values is plotted. This figure uses an instantaneous snapshot of the flow field. (For interpretation of the references to color in this figure legend, the reader is referred to the web version of this article.)

than the dissipation in the Leith simulations, in both quiescent regions and intense dissipation regions. The bottom drag is larger in the QG Leith simulation than in the biharmonic simulation, and this increase is seen in the quiescent regions and in the high bottom drag regions. The bottom drag is proportional to the cubed magnitude of the horizontal bottom velocity, suggesting that the bottom velocities in the Leith simulations are greater than in the biharmonic simulations, consistent with the kinetic energy profiles in Fig. 3 which show that the greatest percentage increase in kinetic energy occurs at the deepest locations. It is likely that the QG Leith simulation is more sensitive to follow-on effects of bottom drag (Arbic and Flierl, 2004). The vertical friction is the largest sink of kinetic energy but there is no significant variation in the magnitude and spatial distribution of the vertical friction term between simulations.

The column-integrated kinetic energy sinks can be horizontally integrated over the global ocean to investigate how the global subgrid kinetic energy sinks are affected by changes in the subgrid scheme. The global rate of kinetic energy dissipation for each depth-integrated sink (*Sink*) was approximated as $\sum_i \rho_0 A_i \text{Sink}$ over all ocean grid points (*i*) each of area A_i using a constant density ($\rho_0 = 1000 \text{ kg m}^{-3}$). Fig. 9 shows the magnitude of these sinks for a snapshot of each simulation. The biggest sink of kinetic energy in

all simulations is through vertical friction within the ocean surface boundary layer. The energy which is not removed by the boundary layer mixing is extracted by dissipation, bottom drag, vertical friction or resolved processes within the ocean interior. The horizontal dissipation of kinetic energy decreases from 0.81 TW in the biharmonic simulation to 0.24 TW in the 2D Leith simulation and 0.27 TW in the QG Leith simulation. The bottom drag increases from 0.19 TW in the biharmonic simulation to 0.34 TW in the 2D Leith simulation and 0.33 TW in the QG Leith simulation. The vertical friction sink in the ocean interior is approximately constant ($\sim 0.25 \text{ TW}$) across all simulations. These results demonstrate that the choice of horizontal mixing scheme can affect the pathways of kinetic energy on a globally integrated scale (Ferrari and Wunsch, 2008). For the biharmonic simulation: horizontal friction \gg interior vertical friction $>$ bottom drag, while in the 2D and QG Leith simulations: bottom drag $>$ interior vertical friction $>$ horizontal friction. A conjecture – not explored here – is that the sensitivity to the vertical friction will be larger under the Leith schemes than under the biharmonic scheme, because the vertical friction is the main parameterized sink of KE in the Leith simulations, therefore increasing the need to accurately parameterize the vertical friction (e.g. MacKinnon et al., 2013).

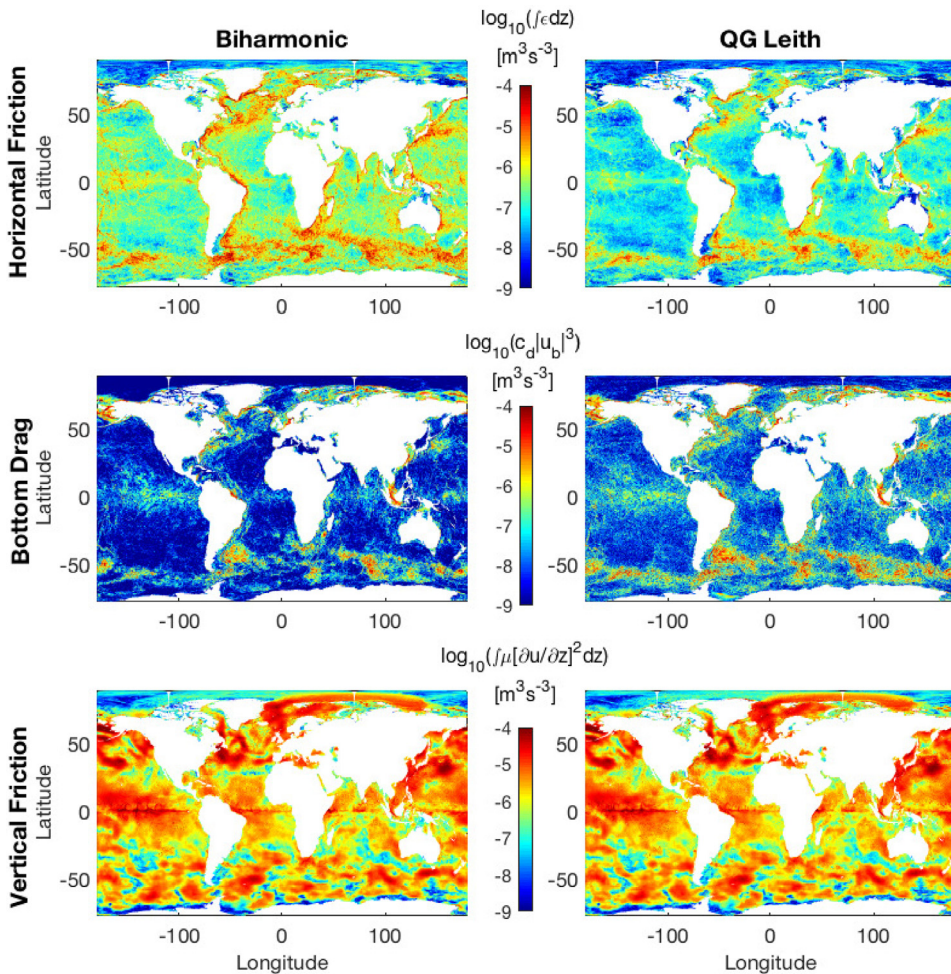


Fig. 8. Maps of kinetic energy sinks, integrated over the depth of the water column, for the biharmonic (left) and QG Leith (right) simulations. Shown are the sinks of KE due to horizontal friction (top), bottom drag (middle) and vertical friction (bottom). Note that the color scales are logarithmic. (For interpretation of the references to color in this figure legend, the reader is referred to the web version of this article.)

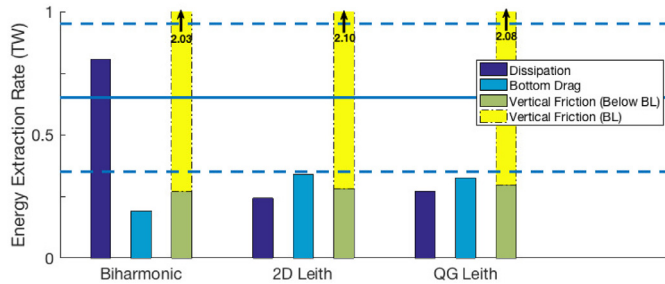


Fig. 9. Global energy extraction rates by dissipation, bottom drag, vertical friction in the boundary layer, and vertical friction below the boundary layer for each simulation. The solid line shows the observed global bottom drag energy extraction calculated by Wright et al. (2013), along with error bars (dotted lines). This figure uses a snapshot of the flow field. (For interpretation of the references to color in this figure legend, the reader is referred to the web version of this article.)

Previous work has shown that spatially variable bottom drag is a large sink of kinetic energy within the ocean, based on observations (Gille et al., 2000; Sen et al., 2008; Wright et al., 2013), non-hydrostatic models (Nikurashin et al., 2013), and theory (Treguier and Hua, 1988; Arbic et al., 2007). In contrast, lateral mixing should be a relatively unimportant sink of energy (Ferrari and Wunsch, 2008). Arbic et al. (2009) showed that 1/10° POP with biharmonic viscosity significantly underestimated bottom drag when compared to observations. Wright et al. (2013) calculated that the

observed global bottom drag extraction of kinetic energy is 0.65 ± 0.3 TW and Sen et al. (2008) showed that the rate was at least 0.4 TW. Using the new QG Leith and 2D Leith parameterizations increases the agreement between the model and observations of global bottom drag extraction of kinetic energy (Fig. 9), even without the use of sophisticated tidal bottom drag parameterizations (Jayne, 2009).

3.5. Mass transport

In the previous sections we have shown that the choice of subgrid scheme can affect ocean energetics, particularly at small scales, but it is also interesting to see how the choice of subgrid scheme affects larger scale properties of the ocean flow. Fig. 10 shows timeseries of mass transports through three different regions for the final four years of each simulation. The three regions were chosen for their disparate driving mechanisms.

The mass transport through Drake Passage is a measure of the strength of the ACC (Cunningham et al., 2003). In the 2D Leith and QG Leith simulations the Drake Passage mass transport is approximately 10% smaller than that of the biharmonic simulation through most of the year - indicative of a reduced ACC. The ACC is sustained by a strong meridional temperature gradient, and its associated thermal wind (Nowlin and Klinck, 1986), and mesoscale eddies play an important role in ACC dynamics (Johnson and Bryden, 1989; Radko and Marshall, 2006). Stronger mixing in ocean models leads to a weaker ACC (Gent et al., 2001), and previ-

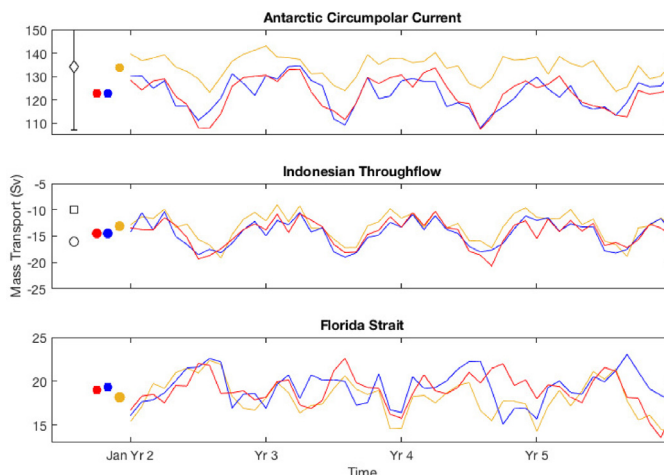


Fig. 10. Timeseries of mass transport through several passages in each simulation. Shown are the ACC mass transport through Drake Passage (top), Indonesian Throughflow (middle) and mass transport through the Florida Strait (bottom) for the QG Leith (red), 2D Leith (blue) and biharmonic (orange) simulations. The transport is calculated from monthly averaged velocity fields. Positive values denote an Eastward transport. Circles denote the mean transport, and the standard error on each mean is within the diameter of each circle. An example of the observed Drake Passage mass transport is shown as a black diamond, where the error bars denote the error on the mean (Whitworth et al., 1983; Whitworth and Peterson, 1985; Cunningham et al., 2003). Observations of the Indonesian Throughflow are shown as a square (Gordon, 2001) and circle (Ganachaud and Wunsch, 2000). (For interpretation of the references to color in this figure legend, the reader is referred to the web version of this article.)

ous studies have shown that the ACC responds to forcing variation differently in eddy-resolving ocean models versus coarse resolution ocean models (Hallberg and Gnanadesikan, 2006; Munday et al., 2013). Danabasoglu and McWilliams (1995) and Kuhlbrodt et al. (2012) showed that increased eddy buoyancy transport (μ_{gm} , Eq. (13)) tended to reduce isopycnal slopes and decrease the ACC transport in coarse resolution simulations. In contrast to Kuhlbrodt et al. (2012), the present simulations are eddy-resolving and the reduction in parameterized viscosity and mixing leads to an increase in resolved mesoscale eddy activity (Fig. 5) and associated buoyancy transport. Fig. 10 shows that in an eddy-resolving model, the combined effect of stronger resolved mesoscale eddy field and weaker subgrid eddy buoyancy transport in the Leith simulations, relative to the biharmonic simulation, results in a weaker ACC.

The magnitude of mass transports through both the Indonesian Throughflow and Florida Strait are affected by the choice of subgrid scheme, but the changes are not as great as that of the Drake Passage transport. The 2D Leith and QG Leith schemes increase the magnitude of the Florida Straits mass transport and the Indonesian Throughflow as compared to the biharmonic simulation. The Indonesian Throughflow is predominantly driven by the pressure gradient between the Pacific and Indian Ocean basins (Wyrtki, 1987; Sprintall and Révelard, 2014) and, on shorter timescales, the excitation of planetary waves (McClean et al., 2005). A frictional transformation of potential vorticity is required for the flow to cross the equator via the throughflow (Edwards and Pedlosky, 1998), so paradoxically larger friction may lead to larger transport (Jochum et al., 2009). In high-resolution models, the Florida Current is driven by a mixture of Rossby and Kelvin waves (Pedlosky, 1965; Czeschel et al., 2012), concentration of inertial flow (Charney, 1955), and bottom torques (Hughes and De Cuevas, 2001; Yeager, 2015). These phenomena should not be strongly affected by the presence, or lack, of resolved mesoscale eddies or weak viscosity at these low latitudes. Therefore, it is unsurprising that they are only weakly sensitive to the choice of subgrid scheme.

The simulations have mass transports which are consistent with observations for the Drake Passage transport and Indonesian Throughflow. But it should be noted that the uncertainties in the observations (where available) are large, and the simulations are not forced using observed forcing for the observation periods. The observed Florida Strait transport is generally larger than all of the simulations (i.e. 32.2 Sv; Baringer and Larsen, 2001). The observations cannot be used to constrain which of the present simulations has the greatest fidelity.

Although the above mass transports are only a subset of the diagnostics which are typically of interest they demonstrate that the choice of subgrid scheme can affect significant and persistent properties such as mass transports, but in a direction and with magnitude that varies with location. Note that the changes in mean mass transports for the Leith simulations relative to the biharmonic simulation are often greater than the standard error, and thus statistically significant.

3.6. Structure functions

One of the aims of the 2D Leith and QG Leith schemes is to improve the fidelity of mesoscale turbulence in GCMs. The fidelity of turbulence in an inertial subrange is often measured using the distribution of properties across different scales, for example through spectral analysis. As discussed in Section 2, theory gives insight into what these features should look like in a high-fidelity simulation. However, methods which require transformation of the flow field to spectral space are not always well-suited to GCMs because of the anisotropy and heterogeneity of the flow, and the uneven grid spacing. There are a limited number of places where closed periodic transects, ideal for spectral analysis, can be easily analyzed (e.g. Fig. 5).

Some of the challenges of spectral analysis can be avoided by instead using physical-space analysis techniques, such as structure functions. Structure functions use correlations between variables at a range of separation distances to describe the spatial structure of turbulence. Similar to turbulence moments, there are hierarchies of structure functions of different orders (Hill, 2001). Here we shall focus on the second-order structure function of a variable (ϕ) for homogeneous turbulence,

$$D_\phi(s) = \overline{[\phi(\mathbf{x} + \mathbf{s}) - \phi(\mathbf{x})]^2}, \quad (18)$$

where s is the magnitude of the horizontal separation vector (\mathbf{s}), and the overline denotes averaging – in this case over all positions, \mathbf{x} , within a specified area (or, in the case of 3D turbulence, a specified volume). In isotropic turbulence, the structure function does not depend on the direction of the separation. Although turbulence in the ocean is heterogeneous, the flow can be approximated as locally homogeneous by only calculating the structure function within small ocean regions – which are still large enough to ensure statistical significance.

Fig. 11 shows the surface salinity structure function for three ocean regions using zonal separation. These regions include mesoscale eddy-dense (ACC), quiescent mid-latitude (NE Pacific) and Equatorial conditions. In the Equatorial Pacific the 2D Leith and QG Leith simulations have larger structure functions at small s , although the differences between simulations are comparable to the interannual variability of the structure functions in this region (gray shading for 2D Leith simulation). In the NE Pacific the 2D Leith simulation has a significantly larger structure function than the other simulations, indicating more small-scale variability than the QG Leith and biharmonic simulations. This is consistent with increased mesoscale turbulence near the grid scale, such as that shown in Figs. 3 and 5. The structure functions in the Equatorial and North Pacific agree reasonably with the observations from Argo drifters (McCaffrey et al., 2015), suggesting that

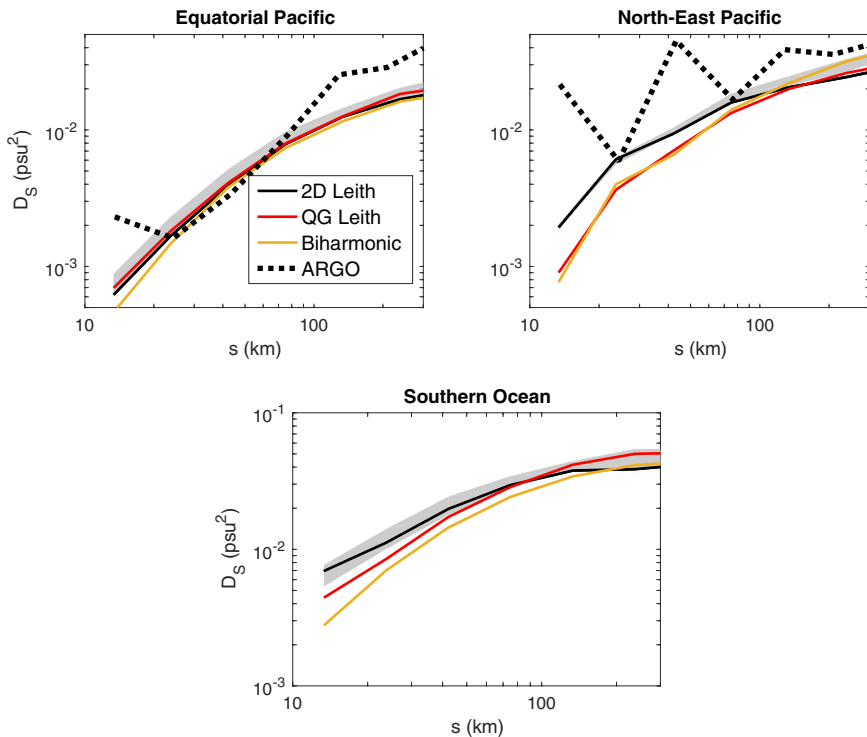


Fig. 11. Salinity structure functions at the surface for (a) Equatorial Pacific, (b) North-East Pacific, and (c) Southern Ocean as a function of zonal separation distance, s , using a snapshot of each simulation. The structure functions are calculated using a zonal separation, s . The Equatorial Pacific region is bound by 10°S, 10°N, 180°W and 150°; the North-East Pacific is bound by 10°N, 30°N, 160°W and 140°W; the Southern Ocean region is bound by 60°S, 40°S, 50°W and 30°W. Gray shading shows the spread in 2D Leith simulations across four years on January 1st. Also shown in (a) and (b) are D_s calculated from ARGO floats (dotted lines), taken from McCaffrey et al. (2015). Note that the ARGO data do not use a specific separation orientation. (For interpretation of the references to color in this figure legend, the reader is referred to the web version of this article.)

model spatial variability is similar to observed variability at the mesoscale. The structure functions using meridional separations (not shown) are larger than the plotted zonal structure functions at all scales although the difference between the two becomes less at smaller separation distances, implying that smaller scale turbulence is more isotropic. This is consistent with an assumption of the LES subgrid schemes; the gridscale lies within an inertial cascade.

The structure functions in the Southern Ocean, which is rich with mesoscale eddies, are an order of magnitude larger than those of the Pacific regions, consistent with the stronger mesoscale eddy field producing more variability at scales below the deformation radius. Both the QG Leith and 2D Leith simulations have larger mesoscale structure functions than the biharmonic simulation in the Southern Ocean. The slope of the structure function of a variable is linearly related to the slope of the variance spectra of that variable (McCaffrey et al., 2015). The structure function should therefore be smooth within an inertial subrange. The 2D Leith and QG Leith simulations both have less curvature in their salinity structure functions than the biharmonic simulation below 100 km, consistent with a more physical inertial subrange of mesoscale turbulence. The differences between structure functions of separate simulations, and the spatial variability of these differences, suggests that structure functions may provide an easy-to-use tool for the analysis of mesoscale turbulence statistics in future studies.

3.7. Effect of GM-Redi vs. horizontal mixing

The Leith simulations differ from the biharmonic simulation by their parameterized mixing strength (ν, κ) and by their tracer mixing orientation (GM-Redi vs. horizontal diffusion). It is therefore pertinent to ask which of these differences is most important in

driving the variations between the Leith simulations and the biharmonic simulation shown in the previous sections. To address this we have carried out a further simulation using horizontal tracer mixing, rather than GM-Redi mixing, with 2D Leith. Snapshots from the horizontal mixing 2D Leith simulation and the GM-Redi 2D Leith simulation are indistinguishable with respect to all the previously plotted variables. Therefore, the differences between the Leith simulations and the biharmonic simulation demonstrated in this paper are a result of the parameterizations for mixing strength (ν, κ, μ_{gm}), and not the along-isopycnal vs. horizontal orientation of tracer mixing.

While Bachman et al. (2017) showed that QG Leith is consistent with the use of GM-Redi tracer mixing, we have not demonstrated that the GM-Redi parameterization offers any benefits over horizontal tracer mixing in a high-resolution simulation. In fact, the computational cost of calculating the isopycnal slopes in GM-Redi is significant (Appendix C). We expect that the (potentially beneficial) effects of being able to use the GM-Redi parameterization will become more apparent when high-resolution simulations are integrated for longer time periods. Over long time scales the along-isopycnal transport of the GM-Redi scheme may cause simulations to diverge from horizontal tracer mixing simulations, because the latter causes diapycnal diffusion where isopycnal surfaces are not horizontal. If computational cost is a limiting factor when choosing subgrid parameterizations, then 2D Leith and QG Leith can be run with horizontal tracer mixing at moderate added cost relative to the standard biharmonic scheme (Appendix C).

The mixing of tracers is also affected by the choice of tracer advection scheme. Bachman et al. (2017) carried out a suite of idealized simulations with multiple tracer advection schemes and found that monotonic schemes can produce numerical diffusion, which can be greater than the parameterized GM-Redi diffusion of the Leith schemes. They obtained the best spectral properties

when a fourth-order, low dissipation tracer advection scheme was used in conjunction with the GM-Redi and QG Leith parameterizations. In the present paper we use a second-order centered advection scheme in the tracer equations, which could induce numerical dispersion, and hence inaccuracies at smaller scales. Unfortunately the options for tracer advection in the POP model are limited to low order schemes. We look forward to future evaluation of the coupling between Leith and tracer advection schemes in longer global ocean simulations.

4. Conclusions

We have implemented two new parameterizations for horizontal mixing by subgrid mesoscale eddies in a high-resolution global ocean model. These two parameterizations are based on large-eddy simulation and are designed to be appropriate for 2D and quasi-geostrophic turbulence (2D Leith and QG Leith, respectively). The new ocean model simulations have been compared to a simulation using a standard biharmonic subgrid scheme. A common feature of all these subgrid schemes is that they represent subgrid horizontal mixing through a parameterized viscosity (ν) and diffusivity (κ). The new simulations show better agreement with QG turbulence theory and observations, particularly in the energetics of resolved mesoscale eddies and in the frictional dissipation mechanisms for kinetic energy.

One of the key properties of the 2D Leith and QG Leith schemes is that ν and κ are both flow-aware and scale-aware, which means that the strength of subgrid eddy mixing can vary spatially in both the horizontal and vertical (e.g. strong mixing in the Southern ocean, western boundary currents and upper ocean), and the mixing can automatically adjust to changes in resolution. As an example, the 2D Leith and QG Leith surface viscosities can vary regionally by two orders of magnitude (1 to 100 m² s⁻¹). This is in contrast to standard schemes (such as the biharmonic scheme) which are not flow-aware, and typically have equivalent viscosities which are orders of magnitude greater than the QG Leith and 2D Leith viscosities. The main difference between the 2D and QG Leith schemes is increased subgrid mixing in the upper kilometer of the ocean and below the base of the boundary layer in the latter.

The resolved mesoscale features of the 2D Leith and QG Leith simulations are more consistent with an inertial cascade than those of the biharmonic simulation. Second-order salinity structure functions and a Southern Ocean kinetic energy spectrum show that the new subgrid schemes result in a smoother spectral slope approaching the grid scale - consistent with an inertial cascade in mesoscale turbulence - while the biharmonic subgrid scheme causes too much mixing and damps the energy within the resolved mesoscale flow. As a result, the 2D and QG Leith simulations have 50% more kinetic energy than the biharmonic simulation below 1 km depth, and there is also a moderate increase near the surface.

The differences in flow energetics between simulations are caused by changes in the kinetic energy budget, because horizontal mixing dissipates kinetic energy within the ocean. The 2D and QG Leith subgrid schemes have less horizontal mixing, and therefore less dissipation, than the biharmonic subgrid scheme. This reduced dissipation is compensated by an increase in the extraction of kinetic energy by bottom drag, which is caused by greater abyssal ocean velocities. The 2D Leith and QG Leith simulations are in better agreement with observations of the rate of kinetic energy removal by bottom drag on a global scale (Ferrari and Wunsch, 2008; Wright et al., 2013). The dissipation of kinetic energy by the vertical viscosity is not significantly affected by the choice of horizontal mixing scheme, although vertical viscosity in the surface boundary layer is the biggest parameterized sink of kinetic energy. The relative magnitude of global kinetic energy sinks in

each simulation, neglecting the large vertical mixing in the surface boundary layer, varies from horizontal friction>interior vertical friction>bottom drag in the biharmonic simulation to bottom drag>interior vertical friction>horizontal friction in the Leith simulations.

The choice of subgrid scheme also affects the mass transport through various straits. Different mass transports did not have the same response to changes in the subgrid scheme. The mass transport through Drake Passage was approximately 10% smaller in the 2D Leith and QG Leith simulations relative to the biharmonic simulation, while the magnitudes of the Indonesian Throughflow and Florida Strait transports were slightly larger in the Leith simulations than in the biharmonic simulation. The Drake Passage transport can be explained by the presence of more energetic mesoscale eddies in the Leith simulations (Fig. 5), which reduce the meridional density gradient and the associated thermal wind balance-induced mass transport.

In the present biharmonic simulations the biharmonic mixing parameters were chosen to be the standard value for high-resolution POP simulations. One may arrive at a better solution through exhaustive tuning of the biharmonic mixing parameters, as demonstrated by Bachman et al. (2017) for an idealized frontal spindown, but this tuning is not a trivial exercise in complex ocean models (e.g. Bryan et al., 2007). The Leith schemes have the benefit that they *do not require tuning* because they take into account the resolution and local flow properties.

It appears difficult to diagnose quantitative differences between the 2D Leith simulation and the QG Leith simulation using standard metrics for global model comparison, despite the latter having greater mixing in certain regions. This is in contrast to idealized simulations, where there are significant differences between the Leith subgrid schemes (Bachman et al., 2017). This could be because the idealized simulations model a frontal spindown, where quasi-geostrophic stretching is more important than it is when averaged across the global ocean at all depths. On the other hand, perhaps this just exemplifies the need for new kinds of model evaluation specifically designed to assess high-resolution models, because typical global model evaluations rely on large scale climatology rather than turbulence statistics. Some basic structure function statistics reveal differences between the two Leith subgrid schemes for global ocean simulations, and such metrics could provide a fruitful tool for inter-comparison of high-resolution ocean models.

Acknowledgments

Maintenance and debugging of the biharmonic simulation performed by David Bailey is gratefully acknowledged. We would like to acknowledge high-performance computing support from Yellowstone (ark:/85065/d7wd3xhc) provided by NCAR's Computational and Information Systems Laboratory, sponsored by the National Science Foundation. B.P. and B.F.K. were supported by NSF 1350795 and F.B. by the NSF through its sponsorship of NCAR. We would like to thank three reviewers, whose comments helped clarify and improve this manuscript.

Appendix A. Calculation of 2D Leith and QG Leith viscosity

The 2D Leith viscosity is a function of the local flow field, and is calculated for each grid point using the local vertical vorticity and divergence (Eq. (8)). The QG Leith viscosity is similar to the 2D Leith viscosity, but also depends upon the quasi-geostrophic stretching and planetary vorticity (Eq. (9)). Because of this, the ν_{qg} calculation also includes some asymptotes and approximations to ensure that the quasi-geostrophic terms are only included when they are appropriate, and that the code is computationally efficient.

The quasi-geostrophic vorticity gradient, the left term within the square root of Eq. (9), is implemented in POP as,

$$\nabla_h q_{qg} = \nabla_h(q_{2d} + f) + \mathbf{S}', \quad (\text{A.1})$$

where $\mathbf{S}' = (S'_x, S'_y)$ is the gradient of the quasi-geostrophic stretching (note that subscripts denote x - and y -components rather than derivatives in this appendix). The magnitude of S'_i is constrained by local non-dimensional numbers,

$$S'_i = \min \left[|S_i|, \left| \frac{\nabla_h(q_{2d} + f)}{\max[Bu, Ro^2]} \right| \right] \frac{S_i}{|S_i|}, \quad (\text{A.2})$$

where S_i is the raw value of the quasi-geostrophic stretching, $Ro^2 = \mathbf{u} \cdot \mathbf{u} / (f^2 A)$ is the squared Rossby number, $Bu = N^2 \Delta_z^2 / (f^2 A)$ is the Burger number, Δ_z is the vertical grid spacing, and A is the horizontal grid area. These constraints ensure that the QG Leith viscosity asymptotes to the 2D Leith viscosity in regions that don't follow quasi-geostrophic dynamics, such as barotropic regions, which have small N^2 and large Bu , or regions with large Ro (Bachman et al., 2017).

The x -component of the raw quasi-geostrophic stretching is calculated as,

$$S_x = \frac{\partial}{\partial z} \left[\frac{f}{N^2} \frac{\partial}{\partial z} \left(\frac{\partial b}{\partial x} \right) \right], \quad (\text{A.3})$$

where $b = -g(\rho - \rho_0)/\rho_0$ is the buoyancy, and $\rho_0 = 1 \text{ kg cm}^{-3}$ is the reference density. The y -component of stretching is the same as Eq. (A.3) with x replaced by y . The gradient operator only acts upon the buoyancy in the quasi-geostrophic stretching, rather than the Coriolis and stretching terms, because QG theory assumes a constant background N^2 and f . Taking the gradient of buoyancy also eliminates the contribution from the mean background buoyancy field, isolating the local buoyancy perturbation, b' .

The computational cost of calculating the QG Leith viscosity is higher than that of the 2D Leith viscosity (Appendix C), as the former requires the 3D buoyancy field to calculate N^2 and vertical gradients in \mathbf{S} . Because of this, the QG Leith simulation updates \mathbf{S} once a day while all the other terms in Eq. (9) are updated every time step. The update rate of the QG stretching is faster than the expected timescale of quasi-geostrophic eddies and advection, and so we do not expect this once-a-day update of the stretching to significantly affect our results. It is also the same update rate as the isopycnal slopes used in the GM-Redi parameterization (Eq. (13)).

Appendix B. Sinks of kinetic energy

There are several terms in the model equations (Eq. (3)) which can affect kinetic energy levels. Several of these terms are sign definite sinks of kinetic energy, and these are the terms we focus on here. All of these sinks arise from the friction terms in Eq. (3). The friction terms (F_H and F_V) can be decomposed into three components; horizontal viscosity, vertical viscosity, and boundary conditions. Taking the inner product of the velocity and the momentum budget results in the kinetic energy budget. The vertical friction term in the kinetic energy budget is,

$$\mathbf{u} \cdot \frac{\partial}{\partial z} \left(\mu \frac{\partial \mathbf{u}}{\partial z} \right) = \frac{\partial}{\partial z} \left(\mu \mathbf{u} \cdot \frac{\partial \mathbf{u}}{\partial z} \right) - \mu \frac{\partial \mathbf{u}}{\partial z} \cdot \frac{\partial \mathbf{u}}{\partial z}, \quad (\text{B.1})$$

where μ is the vertical viscosity. When Eq. (B.1) is integrated over the depth of the water column, the second term on the right-hand side is a sink of the zonal kinetic energy, analogous to the horizontal dissipation. We define the dissipation through vertical viscosity, integrated over the depth of the water column,

$$\int_{-z_{H-1}}^{z_1} \mu \frac{\partial \mathbf{u}}{\partial z} \cdot \frac{\partial \mathbf{u}}{\partial z} dz, \quad (\text{B.2})$$

Table C1

Time taken for each simulation to run for one day, normalized by the time taken for the biharmonic (BH) simulation to run one day (104 cpuhrs).

	BH	2D Leith	QG Leith	2D (no GM)	QG (no GM)
Time	1	1.87	1.96	1.28	1.43

where z_1 is the first grid point below the surface and z_{H-1} is the second deepest grid point at a given location to avoid boundary conditions.

The first term on the right-hand side of Eq. (B.1), when integrated over the depth of the water column, introduces boundary condition terms. The surface and bottom boundary conditions in POP are,

$$\mu \frac{\partial}{\partial z}(u, v) \rightarrow (\tau_x, \tau_y) \text{ at } z = 0, \quad (\text{B.3})$$

$$\mu \frac{\partial}{\partial z}(u, v) \rightarrow c_d |\mathbf{u}|(u, v) \text{ at } z = -H, \quad (\text{B.4})$$

where τ_i is the wind stress in the i direction and $c_d = 10^{-3}$ is the bottom drag coefficient. The surface boundary condition introduces $\boldsymbol{\tau} \cdot \mathbf{u}_s$ where \mathbf{u}_s is the surface velocity. This term is not sign-definite. The bottom drag is a sign-definite sink of column-integrated kinetic energy with magnitude $c_d |\mathbf{u}_b|^3$, where \mathbf{u}_b is the velocity of the bottom grid cell.

The dissipation of kinetic energy through horizontal viscosity, integrated over the depth of the water column (H), is given by,

$$\int_{-H}^0 \varepsilon dz = \int_{-H}^0 \nu [(\nabla_h u) \cdot (\nabla_h u) + (\nabla_h v) \cdot (\nabla_h v)] dz, \quad (\text{B.5})$$

$$\int_{-H}^0 \varepsilon dz = \int_{-H}^0 \nu_{bh} [(\nabla_h^2 u)^2 + (\nabla_h^2 v)^2] dz, \quad (\text{B.6})$$

for the Laplacian and biharmonic friction operators respectively. Care must be taken when calculating the Laplacian operators in the biharmonic dissipation (Eq. (B.6)), as they are sensitive to the choice of stencil. The biharmonic dissipation was derived (Eq. (15)) using the vector identity $\psi \nabla^2 \phi = \phi \nabla^2 \psi + \nabla \cdot (\psi \nabla \phi - \phi \nabla \psi)$, where $\psi = u$ and $\phi = \nu_{bh} \nabla^2 u$. The appropriate stencil for the Laplacian on the right-hand side is one which satisfies this vector identity after numerical discretization given that the left-hand side Laplacian uses a 5-point stencil in POP, e.g. $\partial^2 \phi / \partial x^2 \approx (\phi_1 + \phi_{-1} - 2\phi_0) / \Delta_x^2$, where ϕ_θ is ϕ at a point displaced θ along the x -grid. To satisfy this constraint we use the same 5-point stencil to calculate Laplacian terms in the biharmonic dissipation.

Appendix C. Computational cost of each parameterization

To compare the relative computational cost of each subgrid scheme we ran each subgrid scheme from the same starting point, and compared the total time spent for the code to progress one day for each subgrid scheme. As well as the biharmonic, QG Leith and 2D Leith subgrid schemes, we also included simulations of 2D Leith and QG Leith using horizontal (Laplacian) tracer mixing, rather than GM-Redi, to identify how much of the computational cost change is specifically due to the viscosity and diffusivity parameterizations, and how much is due to the type of tracer mixing. The time for each simulation to run one day is shown in Table C1, and all times have been normalized by the biharmonic simulation time (366 s or 104 cpuhrs).

References

- Abernathy, R., Ferreira, D., Klocker, A., 2013. Diagnostics of isopycnal mixing in a circumpolar channel. Ocean Model. 72, 1–16.

- Kirtman, B.P., Bitz, C., Bryan, F., Collins, W., Dennis, J., Hearn, N., Kinter III, J.L., Loft, R., Roussel, C., Siqueira, L., et al., 2012. Impact of ocean model resolution on CCSM climate simulations. *Clim. Dynam.* 39 (6), 1303–1328.
- Klocker, A., Abernathy, R., 2014. Global patterns of mesoscale eddy properties and diffusivities. *J. Phys. Oceanogr.* 44 (3), 1030–1046.
- Kolmogorov, A.N., 1941. Dissipation of energy in locally isotropic turbulence. *Dokl. Akad. Nauk SSSR*. 32, 16–18.
- Kraichnan, R.H., 1967. Inertial ranges in two-dimensional turbulence. *Phys. Fluids* 10 (7), 1417–1423.
- Kuhlbrodt, T., Smith, R.S., Wang, Z., Gregory, J.M., 2012. The influence of eddy parameterizations on the transport of the Antarctic Circumpolar Current in coupled climate models. *Ocean Model.* 52, 1–8.
- Large, W., Yeager, S., 2009. The global climatology of an interannually varying air-sea flux data set. *Clim. Dynam.* 33 (2–3), 341–364.
- Large, W.G., McWilliams, J.C., Doney, S.C., 1994. Oceanic vertical mixing: a review and a model with a nonlocal boundary layer parameterization. *Rev. Geophys.* 32 (4), 363–403.
- Le Traon, P.Y., Klein, P., Hua, B.L., Dibarboure, G., 2008. Do altimeter wavenumber spectra agree with the interior or surface quasigeostrophic theory? *J. Phys. Oceanogr.* 38 (5), 1137–1142.
- Leith, C., 1996. Stochastic models of chaotic systems. *Physica D* 98 (2), 481–491.
- Lengaigne, M., Madec, G., Menkès, C., Alory, G., 2003. Impact of isopycnal mixing on the tropical ocean circulation. *J. Geophys. Res.* 108 (C11).
- Lucas, D., Klein, R., Tannahill, J., Ivanova, D., Brandon, S., Domyancic, D., Zhang, Y., 2013. Failure analysis of parameter-induced simulation crashes in climate models. *Geosci. Model Dev.* 6 (4), 1157–1171.
- Lumpkin, R., Johnson, G.C., 2013. Global ocean surface velocities from drifters: mean, variance, El Niño–Southern Oscillation response, and seasonal cycle. *J. Geophys. Res.* 118 (6), 2992–3006.
- MacKinnon, J., Laurent, L.S., Garabato, A.N., 2013. Diapycnal mixing processes in the ocean interior. In: Siedler, G., Griffies, S., Gould, J., Church, J. (Eds.), *Ocean Circulation and Climate: A 21st Century Perspective*, Vol. 103. Academic Press, pp. 159–184.
- Maes, C., Madec, G., Delecluse, P., 1997. Sensitivity of an Equatorial Pacific OGCM to the lateral diffusion. *Mon. Weather Rev.* 125 (5), 958–971.
- Maltrud, M., Bryan, F., Peacock, S., 2010. Boundary impulse response functions in a century-long eddying global ocean simulation. *Environ. Fluid Mech.* 10 (1–2), 275–295.
- Maltrud, M.E., McClean, J.L., 2005. An eddy resolving global 1/10° ocean simulation. *Ocean Model.* 8 (1), 31–54.
- Manz, P.P., Zanna, L., 2014. Toward a stochastic parameterization of ocean mesoscale eddies. *Ocean Model.* 79, 1–20.
- McCaffrey, K., Fox-Kemper, B., Forget, G., 2015. Estimates of ocean macroturbulence: structure function and spectral slope from argo profiling floats. *J. Phys. Oceanogr.* 45 (7), 1773–1793.
- McClean, J.L., Bader, D.C., Bryan, F.O., Maltrud, M.E., Dennis, J.M., Mirin, A.A., Jones, P.W., Kim, Y.Y., Ivanova, D.P., Vertenstein, M., et al., 2011. A prototype two-decade fully-coupled fine-resolution CCSM simulation. *Ocean Model.* 39 (1), 10–30.
- McClean, J.L., Ivanova, D.P., Sprintall, J., 2005. Remote origins of interannual variability in the Indonesian Throughflow region from data and a global parallel ocean program simulation. *J. Geophys. Res.* 110 (C10).
- McDougall, T.J., 1987. Neutral surfaces. *J. Phys. Oceanogr.* 17, 1950–1964.
- Munday, D.R., Johnson, H.L., Marshall, D.P., 2013. Eddy saturation of equilibrated circumpolar currents. *J. Phys. Oceanogr.* 43 (3), 507–532.
- Nadiga, B.T., Bouchet, F., 2011. The equivalence of the Lagrangian-averaged Navier–Stokes– α model and the rational large eddy simulation model in two dimensions. *Phys. Fluids* 23 (9), 095105.
- Nguyen, A.T., Menemenlis, D., Kwok, R., 2011. Arctic ice-ocean simulation with optimized model parameters: approach and assessment. *J. Geophys. Res.* 116 (C4).
- Nikurashin, M., Vallis, G.K., Adcroft, A., 2013. Routes to energy dissipation for geostrophic flows in the Southern Ocean. *Nat. Geosci.* 6 (1), 48–51.
- Nowlin, W.D., Klinck, J.M., 1986. The physics of the Antarctic Circumpolar Current. *Rev. Geophys.* 24 (3), 469–491.
- Nycander, J., 2011. Energy conversion, mixing energy, and neutral surfaces with a nonlinear equation of state. *J. Phys. Oceanogr.* 41 (1), 28–41.
- Pedlosky, J., 1965. A note on the western intensification of the oceanic circulation. *J. Mar. Res.* 23 (3), 207–209.
- Pezzi, L., Richards, K.J., 2003. Effects of lateral mixing on the mean state and eddy activity of an equatorial ocean. *J. Geophys. Res.* 108 (C12).
- Pietarila Graham, J., Ringler, T., 2013. A framework for the evaluation of turbulence closures used in mesoscale ocean large-eddy simulations. *Ocean Model.* 65, 25–39.
- Pope, S., Chen, Y., 1990. The velocity-dissipation probability density function model for turbulent flows. *Phys. Fluids A* 2 (8), 1437–1449.
- Radko, T., Marshall, J., 2006. The Antarctic Circumpolar Current in three dimensions. *J. Phys. Oceanogr.* 36, 651–669.
- Redi, M.H., 1982. Oceanic isopycnal mixing by coordinate rotation. *J. Phys. Oceanogr.* 12 (10), 1154–1158.
- Roberts, M.J., Banks, H., Gedney, N., Gregory, J., Hill, R., Mullerworth, S., Pardaens, A., Rickard, G., Thorpe, R., Wood, R., 2004. Impact of an eddy-permitting ocean resolution on control and climate change simulations with a global coupled GCM. *J. Climate* 17 (1), 3–20.
- Roberts, M.J., Marshall, D.P., 1998. Do we require adiabatic dissipation schemes in eddy-resolving models? *J. Phys. Oceanogr.* 28, 2050–2063.
- San, O., Staples, A.E., Iliescu, T., 2013. Approximate deconvolution large eddy simulation of a stratified two-layer quasigeostrophic ocean model. *Ocean Model.* 63, 1–20.
- San, O., Staples, A.E., Wang, Z., Iliescu, T., 2011. Approximate deconvolution large eddy simulation of a barotropic ocean circulation model. *Ocean Model.* 40 (2), 120–132.
- Semtner Jr., A.J., Mintz, Y., 1977. Numerical simulation of the Gulf Stream and mid-ocean eddies. *J. Phys. Oceanogr.* 7 (2), 208–230.
- Sen, A., Scott, R.B., Arbic, B.K., 2008. Global energy dissipation rate of deep-ocean low-frequency flows by quadratic bottom boundary layer drag: computations from current-meter data. *Geophys. Res. Lett.* 35 (9).
- Smagorinsky, J., 1963. General circulation experiments with the primitive equations: I. The basic experiment. *Mon. Weather Rev.* 91 (3), 99–164.
- Small, R., Xie, S., O'Neill, L., Seo, H., Song, Q., Cornillon, P., Spall, M., Minobe, S., et al., 2008. Air-sea interaction over ocean fronts and eddies. *Dynam. Atmos. Oceans* 45 (3), 274–319.
- Smith, K., Boccaletti, G., Henning, C., Marinov, I., Tam, C., Held, I., Vallis, G., 2002. Turbulent diffusion in the geostrophic inverse cascade. *J. Fluid Mech.* 469, 13–48.
- Smith, K.S., Marshall, J., 2009. Evidence for enhanced eddy mixing at middepth in the Southern Ocean. *J. Phys. Oceanogr.* 39 (1), 50–69.
- Smith, R., Jones, P., Briegleb, B., Bryan, F., Danabasoglu, G., Dennis, J., Dukowicz, J., Eden, C., Fox-Kemper, B., Gent, P., et al., 2010. The Parallel Ocean Program (POP) reference manual ocean component of the Community Climate System Model (CCSM) and Community Earth System Model (CESM). Rep. LAUR-01853 141.
- Smith, R.D., Maltrud, M.E., Bryan, F.O., Hecht, M.W., 2000. Numerical simulation of the North Atlantic Ocean at 1/10°. *J. Phys. Oceanogr.* 30 (7), 1532–1561.
- Smith, R.D., McWilliams, J.C., 2003. Anisotropic horizontal viscosity for ocean models. *Ocean Model.* 5 (2), 129–156.
- Sprintall, J., Révelard, A., 2014. The Indonesian throughflow response to Indo-Pacific climate variability. *J. Geophys. Res.* 119 (2), 1161–1175.
- Timmermans, M.-L., Cole, S., Toole, J., 2012. Horizontal density structure and restratification of the arctic ocean surface layer. *J. Phys. Oceanogr.* 42, 4, 659–668.
- Treguier, A., Hua, B., 1988. Influence of bottom topography on stratified quasi-geostrophic turbulence in the ocean. *Geophys. Astro. Fluid* 43 (3–4), 265–305.
- Veronis, G., 1975. The role of models in tracer studies. In: *Numerical Models of Ocean Circulation: Proceedings of a Symposium Held at Durham, New Hampshire, October 17–20, 1972*. National Academy of Sciences, pp. 133–146.
- Visbeck, M., Marshall, J., Haine, T., Spall, M., 1997. Specification of eddy transfer coefficients in coarse-resolution ocean circulation models. *J. Phys. Oceanogr.* 27 (3), 381–402.
- Wajcowa, R.C., 1993. A consistent formulation of the anisotropic stress tensor for use in models of the large-scale ocean circulation. *J. Comput. Phys.* 105 (2), 333–338.
- Welch, P.D., 1967. The use of fast Fourier transform for the estimation of power spectra: a method based on time averaging over short, modified periodograms. *IEEE T. Acoust. Speech* 15 (2), 70–73.
- Whitworth III, T., 1983. Monitoring the transport of the Antarctic Circumpolar current at Drake Passage. *J. Phys. Oceanogr.* 13 (11), 2045–2057.
- Whitworth III, T., Peterson, R., 1985. Volume transport of the Antarctic Circumpolar current from bottom pressure measurements. *J. Phys. Oceanogr.* 15 (6), 810–816.
- Williams, G.P., 1972. Friction term formulation and convective instability in a shallow atmosphere. *J. Atmos. Sci.* 29 (5), 870–876.
- Wright, C.J., Scott, R.B., Furnival, D., Ailliot, P., Vermet, F., 2013. Global observations of ocean-bottom subinertial current dissipation. *J. Phys. Oceanogr.* 43 (2), 402–417.
- Wyrtki, K., 1987. Indonesian through flow and the associated pressure gradient. *J. Geophys. Res.* 92 (C12), 12941–12946.
- Yaglom, A., 1966. The influence of fluctuations in energy dissipation on the shape of turbulence characteristics in the inertial interval. *Sov. Phys. Dokl.* 11, 26.
- Yeager, S., 2015. Topographic coupling of the Atlantic overturning and gyre circulations. *J. Phys. Oceanogr.* 45 (5), 1258–1284.
- Young, W.R., 2010. Dynamic enthalpy, conservative temperature, and the seawater Boussinesq approximation. *J. Phys. Oceanogr.* 40 (2), 394–400.
- Zhurbas, V., Oh, I.S., 2003. Lateral diffusivity and Lagrangian scales in the Pacific Ocean as derived from drifter data. *J. Geophys. Res.* 108 (C5).
- Zurita-Gotor, P., Held, I.M., Jansen, M.F., 2015. Kinetic energy-conserving hyperdiffusion can improve low resolution atmospheric models. *J. Adv. Model. Earth Syst.* 7 (3), 1117–1135.